

## Task 1.1

### Title

Resource exploration and characterization

### Projects (presented on the following pages)

Porosity evolution of bioclastic beds during early diagenesis: Upper Muschelkalk, Switzerland  
A. Adams, L. W. Diamond

Anhydrite-dissolution porosity in the Upper Muschelkalk aquifer, NE-Swiss Molasse Basin: implications for geo- energy and gas storage  
L. Aschwanden, A. Adams, L. W. Diamond, M. Mazurek

Seismic transmissivity of fractures from full-waveform sonic log measurements  
N. D. Barbosa, E. Caspari, J. Germán Rubino, T. Zahner, A. Greenwood, L. Baron, K. Holliger

Geothermal prospection in the Greater Geneva Basin (Switzerland and France): Multidisciplinary approach  
M. Brentini, N. Clerc, E. Rusillon, A. Moscariello

Geophysical characterization of a hydrothermally active fault zone in crystalline rocks – GDP 1 borehole, Grimsel Pass project  
E. Caspari, L. Baron, T. Zahner, A. Greenwood, E. Toschini, D. Egli, K. Holliger

Attenuation in fluid-saturated fractured porous media – quasi-static numerical upscaling vs dynamic wave propagation modeling  
E. Caspari, M. Novikov, V. Lisitsa, N. Barbosa, B. Quintal, J. Germán Rubino, K. Holliger

Fault structure and porosity distribution in an active hydrothermal system  
D. Egli, R. Baumann, S. Küng, A. Berger, L. Baron, M. Herwegh

Characterization and imaging of a fractured crystalline hydrothermal fault zone from hydrophone VSP data  
A. Greenwood, E. Caspari, J. Hunziker, L. Baron, K. Holliger

Gravity survey in the Geneva Basin for deep geothermal and heat storage projects  
L. Guglielmetti, G. Mijic, A. Moscariello, D. Dupuy, P. Radogna

VSP Survey at the Thonex Well, Geneva  
L. Guglielmetti, A. Moscariello, M. Francois, C. Nawratil de Bono, C. Dezayes, B. Adnand, P. Corubolo, F. Poletto

Seismic attenuation in porous rocks containing stochastic fracture networks  
J. Hunziker, M. Favino, E. Caspari, B. Quintal, J. Germán Rubino, R. Krause, K. Holliger

Towards fracture characterization using tube waves  
J. Hunziker, S. Minato, E. Caspari, A. Greenwood, K. Holliger

Importance of the dolomitization of Upper Jurassic carbonate rocks for geothermal prospection in the Geneva Basin (Switzerland & France)  
Y. Makhloufi, E. Rusillon, M. Brentini, M. Meyer, E. Samankassou

Investigations of the evolution in physical properties of crustal rocks with different degree of microfracturation  
L. Pimienta, M. Violay

A numerical approach for studying attenuation in interconnected fractures  
B. Quintal, E. Caspari, K. Holliger, H. Steeb

Quantification of the 3D thermal anomaly of the orogenic geothermal system at Grimsel Pass  
C. Wanner, L. W. Diamond, P. Alt-Epping

Causes of abundant calcite scaling in geothermal wells in the Bavarian Molasse Basin, Southern Germany  
C. Wanner, F. Eichinger, T. Jahrfeld, L. W. Diamond

Measuring pressure dependent fracture aperture distribution in rough walled fractures using X-ray computed tomography  
Q. C. Wenning, C. Madonna, L. Joss, R. Pini

**Porosity evolution of bioclastic beds during early diagenesis: Upper Muschelkalk, Switzerland**

A.Adams<sup>1</sup>; L.W. Diamond<sup>1</sup>

1) Rock-Water Interaction Group, Institute of Geological Sciences, University of Bern, Baltzerstrasse 1+3, CH-3012 Bern, Switzerland

**1. Introduction**

The Middle Triassic Upper Muschelkalk of the Swiss Molasse Basin is under study as a potential gas storage reservoir and for geothermal energy production. It is characterized by a porous upper dolomitic unit (Trigonodus Dolomit) and a tight lower calcitic unit (Hauptmuschelkalk). Porosities of the Swiss Hauptmuschelkalk are <5% on average, however in Germany the Hauptmuschelkalk reaches porosities over 20%.

Using cathodoluminescence (CL), UV-fluorescence (UV-F), stable isotopes and point counting, four diagenetic environments were identified in boreholes across northern Switzerland. The same paragenetic sequence occurred at all depths in each borehole. The results shed light on the improbability of any porous bioclastic beds in Switzerland.

**2. Results**

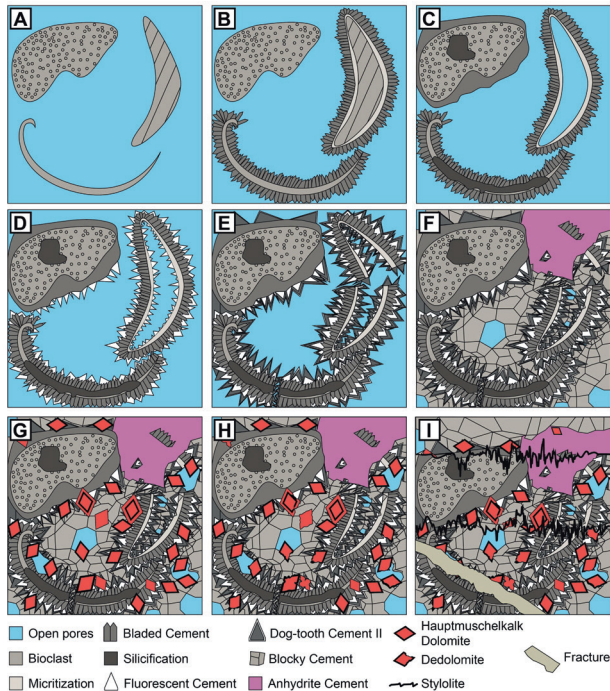


**Figure 1) Schematic diagrams of early diagenesis**

**Marine diagenesis**

- A) Initial deposition of a crinoid (left), aragonitic bivalve (right) and brachiopod (bottom).
- B) Micritization and bladed cement.

**Mixing-zone diagenesis**

- C) Silicification and inclusion-rich syntaxial cement.
- D) Leaching and fluorescent dog-tooth cement.

**Meteoric diagenesis**

- E) Dull and bright dog-tooth cement, and compaction.
- F) Blocky cement and anhydrite cement.

**Shallow burial diagenesis**

- G) Dissolution and subsequent Hauptmuschelkalk dolomitization.
- H) Dedolomitization.
- I) Stylolitization and fracturing cutting all features.

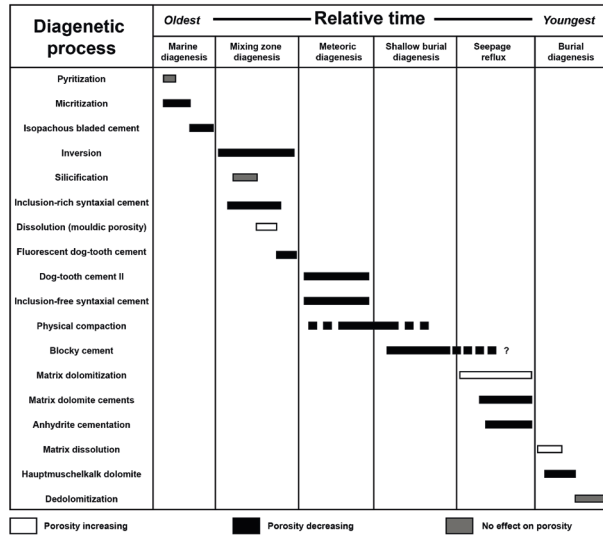


**Figure 2) Summary of early diagenetic events**

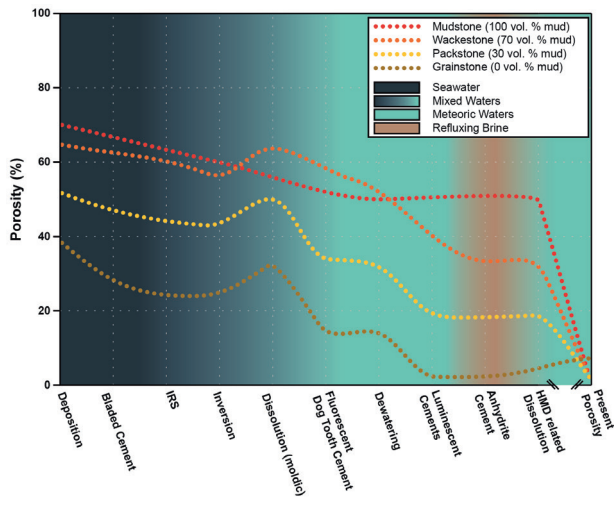


**Figure 3) Quantification of porosity in relation to early diagenetic events**

Porosities of bioclastic beds were calculated based on thin-section point counting and a fixed mud vol. % with a porosity of 70%. Background colours refer to pore fluids during diagenesis.

**3. Conclusions and Outlook**

- Early diagenesis of the Upper Muschelkalk resulted from 18 diagenetic events prior to stylolitization.
- Meteoric cementation caused the most significant occlusion, often by a more than 50% relative reduction in porosity.
- Bioclast hosted and derived porosities were already <5% prior to significant burial.
- More suitable reservoir conditions may exist where there was less influence from meteoric waters. This however, may prove to be only in southern Germany.

# Anhydrite-dissolution porosity in the Upper Muschelkalk aquifer, NE-Swiss Molasse Basin: implications for geo-energy and gas storage

L. Aschwanden, A. Adams, L.W. Diamond, M. Mazurek

Rock-Water Interaction Group, Institute of Geological Sciences, University of Bern, Baltzerstrasse 1+3, CH-3012 Bern, Switzerland

In cooperation with the CTI

Energy Swiss Competence Centers for Energy Research

Schweizerische Eidgenossenschaft  
Confédération suisse  
Confederazione Svizzera  
Confederaziun svizra  
Swiss Confederation

Commission for Technology and Innovation CTI

## Introduction

In the Swiss Molasse Basin (SMB; Fig. 1), deep saline aquifers are one of the options under investigation for geothermal energy production and for geological storage of gas. Particularly the Middle Triassic dolomites within the Upper Muschelkalk (Trigonodus Dolomit) show encouraging aquifer properties along the northern margin of the SMB.

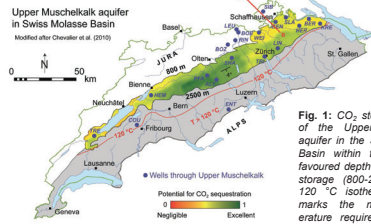


Fig. 1: CO<sub>2</sub> storage potential of the Upper Muschelkalk aquifer in the Swiss Molasse Basin within the technically favoured depth range for CO<sub>2</sub> storage (800-2500 m). The 120 °C isotherm (red line) marks the minimal temperature required to produce geothermal electricity.

Matrix porosity and permeability are locally high (<25% and <100 mD, respectively), in part due to beds rich in cm-dm scale cavities left by the dissolution of eogenetic anhydrite nodules (Fig. 2). However, the spatial distribution of anhydrite-dissolution pores is not well known as the basin is underexplored. The present study reconstructs the genesis and evolution of these pores, thus providing conceptual understanding to support ongoing exploration.



Fig. 2: Drill-core section of the Trigonodus Dolomit at the BEN borehole. The cm-dm scale cavities originate from the dissolution of eogenetic anhydrite nodules.

## Methods

The reconstruction of the genesis and evolution of the anhydrite-dissolution cavities is based on drill-core samples from various boreholes across the Swiss Molasse Basin and it includes:

- Standard petrographic investigations
- Analyses of stable and radiogenic isotopes (i.e. δ<sup>2</sup>H, δ<sup>18</sup>O, and <sup>87</sup>Sr/<sup>86</sup>Sr) of rock-forming (dolomite) and pore-filling (quartz, calcite and kaolinite) minerals
- Fluid inclusion studies of pore-filling quartz and calcite

## Petrography

Some of the anhydrite-dissolution cavities have been affected by two events of mineral precipitation: (1) precipitation of quartz during anhydrite dissolution; (2) a second, younger event in which calcite and kaolinite co-precipitated.

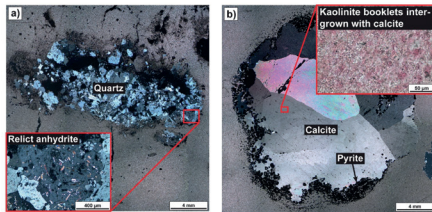


Fig. 3: Thin-section microphotographs of (a) pore-filling quartz with solid inclusions of relict anhydrite and (b) of paragenetically younger pore-filling calcite intergrown with kaolinite.

## Fluid inclusion studies

Primary saline water and methane inclusions were trapped simultaneously in both quartz and younger calcite. Homogenisation temperatures are therefore equivalent to trapping temperatures (Fig. 4a).

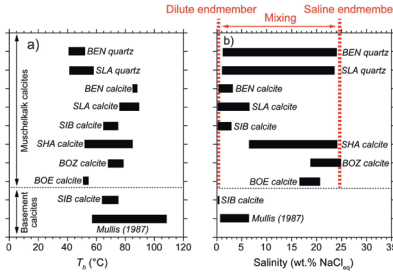


Fig. 4: Microthermometric results of primary fluid inclusions in pore-filling minerals. Salinity is based on ice-melting temperatures.

## Isotope analyses

Pore- and fracture-filling calcite in the Upper Muschelkalk yield high <sup>87</sup>Sr/<sup>86</sup>Sr ratios relative to the dolomite matrix. These high values overlap with the <sup>87</sup>Sr/<sup>86</sup>Sr signatures of basement water and calcite fracture-fillings.

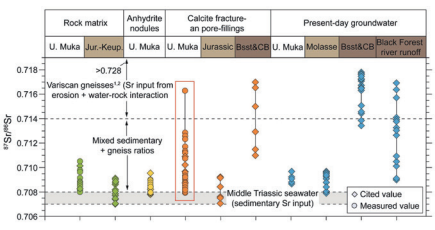


Fig. 5: Strontium isotope ratios for rock matrix, anhydrite nodules, secondary pore- and fracture fillings and the recent groundwater in the Muschelkalk and in its overlying (beige) and underlying (brown) units (Bsst: Buntsandstein; CB: Variscan gneiss basement; Pearson et al., 1991; Nagra, 2001; McArthur et al., 2001; Durand et al., 2005).

## Isotope analyses

Stable and radiogenic isotopes show that the original hypersaline porewater of the Muschelkalk was diluted by infiltration of meteoric water containing radiogenic Sr. This water overlaps with the δ<sup>18</sup>O-δ<sup>2</sup>H of basement waters.

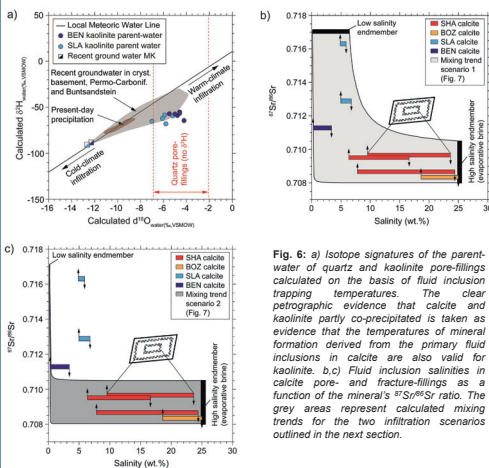


Fig. 6: a) Isotope signatures of the parent-water of quartz and kaolinite pore-fillings calculated on the basis of fluid inclusion trapping temperatures. The clear petrographic evidence that calcite and kaolinite partly co-precipitated is taken as evidence that the temperatures of mineral formation derived from the primary fluid inclusions in calcite are also valid for kaolinite. b,c) Fluid inclusion salinities in calcite pore- and fracture-fillings as a function of the mineral's <sup>87</sup>Sr/<sup>86</sup>Sr ratio. The grey areas represent calculated mixing trends for the two infiltration scenarios outlined in the next section.

## Discussion

Fluid inclusion and isotope evidence shows that anhydrite was dissolved by influx of meteoric water with high <sup>87</sup>Sr/<sup>86</sup>Sr ratios.

The only feasible sources of radiogenic Sr in the local stratigraphy are the underlying Buntsandstein and Variscan gneiss basement (Fig. 7).

Two scenarios are conceivable for the path of infiltration (Fig. 7)

Calculated mixing trends for calcite parent-waters show that mixing of a hypersaline, strontium-rich brine with low-salinity, strontium-poor meteoric runoff from the Black Forest Highlands cannot explain the intermediate salinity of primary fluid inclusions in the radiogenic secondary calcites at the BEN and SLA wells. In contrast, mixing with strontium-enriched basement water explains the observations.

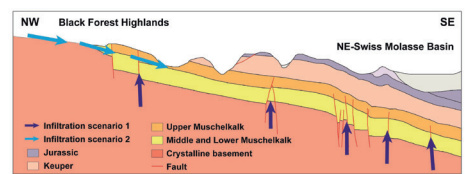


Fig. 7: Water modified by the interaction with crystalline basement rocks could have infiltrated the Upper Muschelkalk according to two different scenarios: (1) fluid ascent along cross-formational faults or (2) lateral recharge of meteoric runoff from the Black Forest Highlands, where the basement rocks are exhumed (see Fig. 1 to locate the profile, modified after Müller et al., 2002).

## Conclusions

Anhydrite-dissolution porosity in the Muschelkalk was caused by the incursion of groundwater from the underlying crystalline basement and/or the Buntsandstein, which ascended along cross-formational faults. Accordingly, anhydrite-dissolution porosity is spatially restricted to the vicinity of deep-seated tectonic structures, which hydraulically connect the crystalline basement and the Muschelkalk. This finding should aid in focussing geothermal and gas-storage exploration in the Swiss Molasse Basin.

## Seismic transmissivity of fractures from full-waveform sonic log measurements

Nicolás D. Barbosa<sup>1</sup>, Eva Caspari<sup>1</sup>, J. Germán Rubino<sup>2</sup>, Tobias Zahner<sup>1</sup>, Andrew Greenwood<sup>1</sup>, Ludovic Baron<sup>1</sup>, and Klaus Holliger<sup>1</sup>

1- University of Lausanne  
2- CONICET, Centro Atómico Bariloche

### Introduction

The identification and proper characterization of fractures is of increasing concern in many domains ranging from hydrocarbon exploration to CO<sub>2</sub> sequestration and nuclear waste storage. In the case of fractured crystalline rocks, such as those prevailing in petrothermal reservoirs, the impact of the fractures on the mechanical and hydraulic properties is particularly strong. Acoustic attributes from full-waveform sonic (FWS) logs are suitable for the identification of fractures. However, the quantitative determination of their mechanical and hydraulic properties is not straightforward as FWS measurements represent averages over intervals that tend to be much larger than the fracture thickness. In this work, we propose a novel methodology to determine the transmission coefficient associated with a single thin layer, such as a fracture, or a vein based on attenuation and phase velocity estimations from FWS. This quantity can be then directly related to the normal compliance of the thin layer, which is a key mechanical parameter.

### FWS data acquisition

FWS data were acquired at the Grimsel Felslabor INJ2 borehole using a single transmitter and three receivers at nominal frequencies of 3, 15, and 25 kHz. In order to increase the signal-to-noise ratio, we performed multiple static measurements at each position and subsequently stacked them. In addition, by considering multiple source-receiver offset configurations, we can estimate the geometrical spreading correction associated to the probed borehole environment. To this end, we have considered two tool configurations, "short" and "long" (Fig. 1).

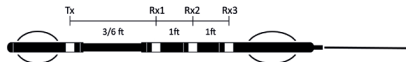


Fig.1: Sonic log tool with one transmitter (Tx) and three receivers (Rx1, Rx2, Rx3).

The offset to the source of the first receiver is 3 and 6 ft for the "short" and "long" tool configurations, respectively.

### Velocity and attenuation estimation from FWS data

In order to compute P-wave attenuation and velocity, we have separated the head P-wave arrival from later arrivals using a tapered time window. For each interval between receivers, we have determined phase velocities  $v_p$  by calculating the phase difference  $\Delta\phi$  from the unwrapped phase spectrum of the corresponding recorded signals

$$v_p(\omega) = \frac{\omega \Delta r}{\Delta\phi(\omega)} \quad (1)$$

where  $\omega$  is the angular frequency and  $\Delta r$  the distance between receivers. Fig. 2 shows the phase velocity profile in the upper section of the borehole. Some velocity dispersion is evident from the difference between the velocities for 15 and 25 kHz. Notice that the presence of fractures, slightly reduces the effective velocity of the medium. Some erratic behavior of the velocity profile has been attributed to damaged zones in the borehole based on televiwer images.

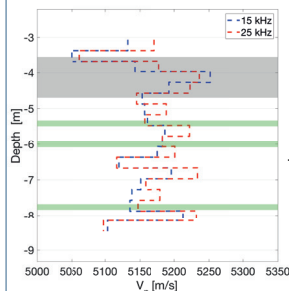


Fig. 2: Velocity profile computed from 15 and 25 kHz measurements. Grey zone corresponds to ductile shear zones. Green features are fractures.

$$Q_p^{-1}(\omega) = \ln \left( \frac{A(\omega, r_i) G_{i+1}}{A(\omega, r_{i+1}) G_i} \right) \frac{2v_p(\omega)}{\omega \Delta r} \quad (2)$$

where  $A(\omega, r_i)$  is the head P-wave spectrum at the  $i$ th-receiver and  $G_i$  is the geometrical spreading function, which depends on frequency, position, and source-receiver offset.

### Transmission losses determination

The attenuation in Eq. 2 can be expressed as

$$Q_p^{-1}(\omega) = Q_{spread}^{-1}(\omega) + Q_{int}^{-1}(\omega) + Q_{transm}^{-1}(\omega) \quad (3)$$

where  $1/Q_{spread}$ ,  $1/Q_{int}$ , and  $1/Q_{transm}$  refer to the attenuation associated with the geometrical spreading, the intrinsic loss of the formation, and the transmission loss associated to the presence of interfaces and layers in the formation.

Assuming that, in Eq. 3, only  $Q_{spread}$  depends on the offset between the source and receivers and that  $G_i = (1/r_i)^\gamma$ , we can use the raw attenuation measurements from different tool configurations (Fig.1) to estimate the geometrical spreading correction (Fig. 3).

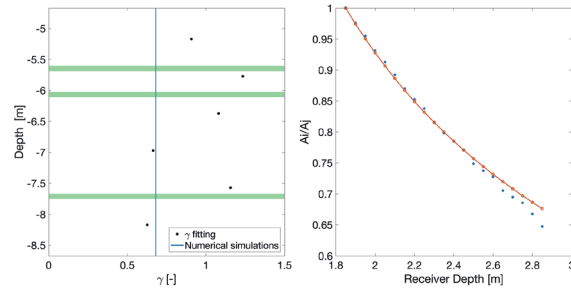


Fig.3: Geometrical spreading correction factor  $\gamma$  obtained from the combination of long and short offset configurations at 25 kHz (left) and from numerically simulated log data (right). For the numerical simulations, the parameters of the medium were chosen based on measurements on core samples characterizing the host granodiorite and using sonic velocities for P- and S-waves.

The attenuation depth profiles after geometrical spreading correction are shown in Fig. 4. From the standard deviation of the fitting of  $\gamma$ , we have defined a range of possible values of corrected attenuation. From the attenuation depth profile, we identify a reference value for the background intrinsic attenuation.

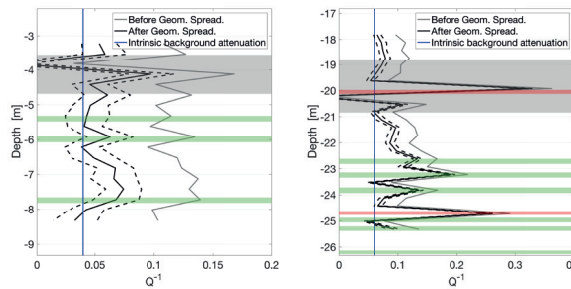


Fig.4: Attenuation profile for 25 kHz sonic log data. Blue curve is identified as the intrinsic background attenuation. Grey, red and green zones correspond to ductile shear, dyke, and fracture sections, respectively.

For each receiver interval, we can compute an effective P-wavenumber from the attenuation and velocity estimations as

$$k_p^{eff}(\omega) = \frac{\omega}{v_p(\omega)} \left( 1 - i \frac{Q_p^{-1}(\omega)}{2} \right) \quad (4)$$

In addition, the background reference velocity and attenuation can be used to obtain a P-wavenumber of the background rock  $k_p^b$ . Finally, the transmission coefficient of a thin layer can be approximated as

$$A_i(\omega) = e^{i(k_p^b - k_p^{eff})\Delta r} \quad (5)$$

from which normal compliance values can be estimated. This effective quantity of the thin layer responsible of the transmission losses, can be used to obtain information on the material composing it. We have verified this for the dykes and veins for which the estimated velocities are close to those found in the literature for lamprophyres and quartz, respectively.

### Conclusions

We have presented a novel approach that allows us to estimate the transmissivity of a single thin layer using FWS log data. The advantage of estimating transmission coefficients of thin-layer-type structures such as veins or fractures, is that it allows us to isolate and quantify their mechanical properties.

### Acknowledgements

This work has been completed within the Swiss Competence Center on Energy Research – Supply of Electricity with the support of the Swiss Commission for Technology and Innovation.

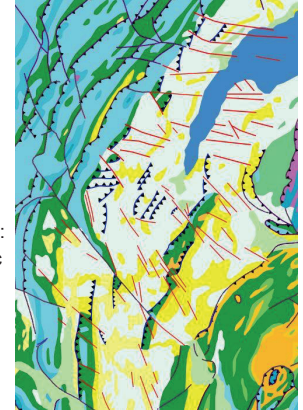
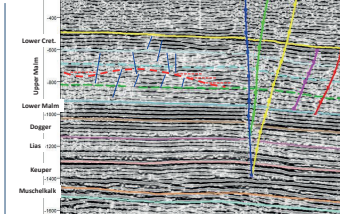
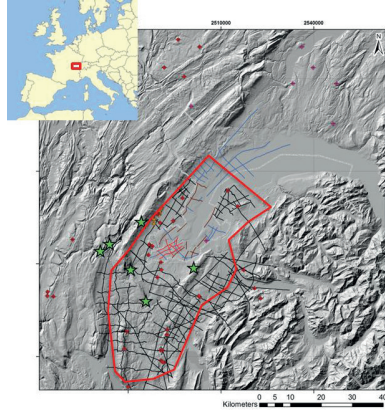
# Geothermal prospection in the Greater Geneva Basin (Switzerland and France): Multidisciplinary approach

Maud Brentini (\*), Nicolas Clerc (\*), Elme Rusillon (\*), Andrea Moscariello (\*)

(\* Department of Earth Sciences, University of Geneva, 13 rue des Maraichers, 1205 Geneva (maud.brentini@unige.ch)

## Introduction

**G**eneva  
**E**nergy  
**O**bjectif  
**T**ectonic  
**H**ydrolic  
**E**lectricity  
**R**esources  
**M**ultidisciplinary  
**I**nvestigation  
**E**valuation  
**2 0 2 0**



### Massive calcareous Upper Malm units:

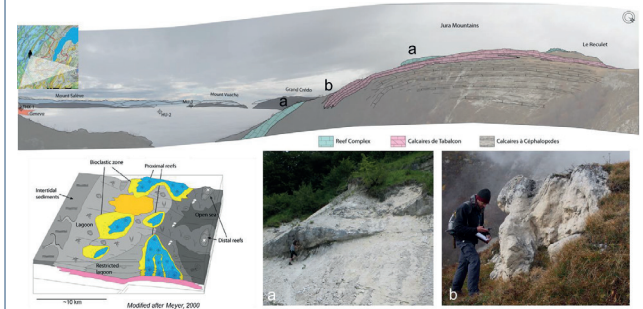
- Often chaotic / discontinuous seismic facies  
→ fracture-enhanced permeability zones?
- Dome-shape structures surrounded by overlapping reflectors within the Kimmeridgian interval  
→ reef structures?

The GEothermie2020 program, managed by the State of Geneva and implemented by the SIG (Services Industriels de Genève), aims at developing geothermal energy resources in the Greater Geneva Basin (GGB). A reservoir assessment has been then performed in the Greater Geneva Basin to evaluate the geothermal resources potential of low to medium enthalpy. For this purpose, a detail structural analysis of the basin has been carried out simultaneously with a reservoir appraisal study including petrophysical properties assessment in a consistent sedimentological and stratigraphical frame.

This multi-disciplinary study has been organized in 4 steps:

- (1) Investigation of the surrounding outcrops to understand the stratigraphy and lateral facies distribution of the sedimentary sequence from Permo-Carboniferous to Lower Cretaceous units
- (2) Development of 3D geological models derived from 2D seismic and well data focusing on the structural scheme of the basin to constrain better the tectonic influence on facies distribution and to assess potential hydraulic connectivity through faults between reservoir units
- (3) Evaluation of the distribution, geometry, sedimentology and petrophysical properties of potential reservoir units from well data
- (4) Identification and selection of the most promising reservoir units for in-depth rock type characterization and 3D modeling.

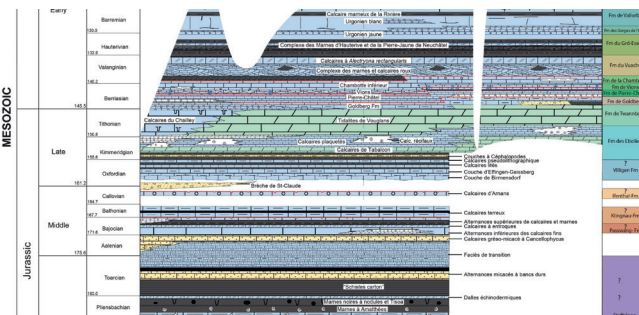
Current fault framework interpretation from 2D seismic data in the Geneva and surrounding basins reveals strike-slip fault segments oscillating between two main directions: SSE-NNE in the southern and central parts & E-W in the northern part and toward the foothills of the Jura. Intra-basinal smaller scale thrust faults appear restricted to the more brittle calcareous-prone units of the Upper Jurassic and Lower Cretaceous units whereas deeper (marl-prone) Mesozoic units deform in a more ductile manner.



## Stratigraphic framework

### Challenge

- Harmonization of the stratigraphy of the Geneva Basin
- Establishment of composite logs
- Correlation with national stratigraphy (HARMOS)
- Implementation of stratigraphic catalog



### Main issues

- Heterogeneities and discrepancies of data
- Important lateral variabilities

### The Kimmeridgian Reef complex

- Most promising geothermal reservoir
- Complex facies architecture and petrophysical properties distribution
- Prevailing microporosity
- Increasing fracture density in the Reef complex and in dolomitized intervals
- Identification of zones of fracture-enhanced permeability on seismic data and outcrops

### Conclusion

- ✓ Definition of a stratigraphic catalog with a clear stratigraphic framework for the GGB.
- ✓ Lateral extent and precise orientation of seismic-scale faults remains challenging with current 2D seismic dataset
- ✓ Better understanding of the distribution and properties of productive reservoir facies as well as hydraulic connectivity zones within the study area.
- ✓ Petrophysical investigations revealed that the Kimmeridgian-Tithonian Reef Complex and the underlying Calcaires de Tabalcon units are the most promising geothermal reservoir targets
- ✓ Kimmeridgian reef buildups are tentatively interpreted on 2D seismic as being responsible for the dome-shape structures observed across the basin.
- ✓ Consistent knowledge for future geothermal exploration pushes toward the successful development of this sustainable energy resource in the GGB.

# Geophysical characterization of a hydrothermally active fault zone in crystalline rocks – GDP 1 borehole, Grimsel Pass project

Eva Caspari<sup>1</sup>, Ludovic Baron<sup>1</sup>, Andrew Greenwood<sup>1</sup>, Tobias Zahner<sup>1</sup>, Enea Toschini<sup>1</sup>, Daniel Egli<sup>2</sup> and Klaus Holliger<sup>1</sup>,  
*University of Lausanne and University of Bern*

In cooperation with the CTI

**Energy**  
Swiss Competence Centers for Energy Research

Schweizerische Eidgenossenschaft  
Confédération suisse  
Confederazione Svizzera  
Confederaziun svizra

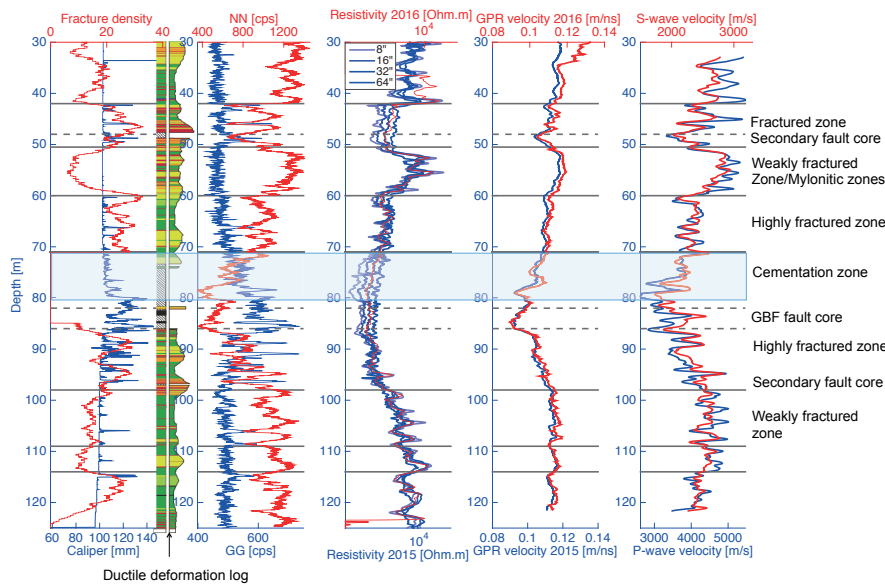
Swiss Confederation  
Commission for Technology and Innovation CTI

**70** Energy Turnaround  
National Research Programme

## Motivation

A shallow near-vertical hydrothermally active fault zone embedded in sheared and fractured crystalline rocks of the Central Aar massif (Switzerland), has been drilled and geophysically explored in view of its potential analogies to planned deep natural geothermal reservoirs in the Alpine Foreland. The geophysical well logs collected in 2015 (open hole) and 2016 (screened hole) characterize the petrophysical variations of the Grimsel Breccia Fault (GBF) due to ductile and brittle deformation in the fault core and the surrounding damage zones. Open fracture porosity estimates obtained from the nuclear and borehole radar logs correlate well with the petrophysical variations observed.

## Borehole logging data

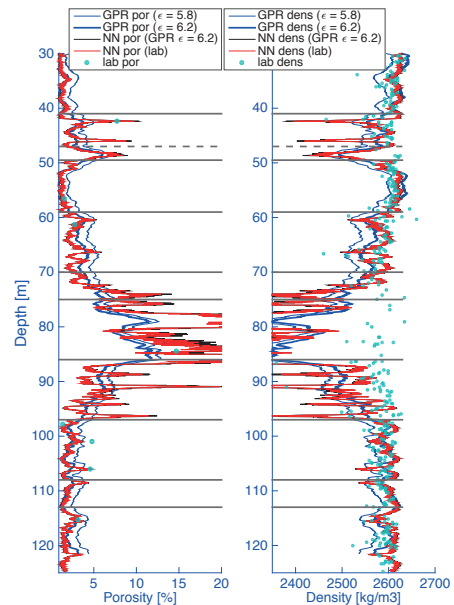


A selection of geophysical logging data acquired during 2015 (open hole) and 2016 (screened casing) is shown alongside fracture density and relative deformation intensity logs (first column) obtained from core analysis and televiewer data. The geophysical logging data comprise nuclear (neutron-neutron NN and gamma-gamma GG) and resistivity logs and borehole ground-penetrating radar (GPR) and sonic (P- and S-wave) velocities. The main trend is consistent for all logs and correlates well with the degree of deformation and fracturing of the formation and the GBF fault core is clearly delineated. The resistivity logs have low values in the highly fractured zones. This is expected since they are directly sensitive to the water content of the formation (electrolytical conductivity) and thus to open fracture porosity. However, large variabilities of the resistivity logs can be observed in zones of low fracture density (e.g. 50-60 m depth). This, together with the overall low resistivity values for a granitic formation within these zones, is indicative of the presence of surface conductivity, most likely due to the abundance of mica in the mylonites.

## Porosity and density estimates

Borehole radar, neutron-neutron and resistivity logs are suitable for the estimation of porosity and the gamma-gamma log is classically utilized to derive densities. However, the GG log is strongly affected by the large variations in borehole diameter, depicted by the caliper log, which caused calibration issues and thus reliable density estimates are not possible. To constrain the density, Archimedes-type density measurements (Lab dens) performed on core samples taken at 20-30 cm intervals over the entire borehole length are utilized. The upper bound of density is well constrained by low cleavage and non fractured Grimsel Granite samples taken at 55 and 120 m depth. However, the lower bound is less reliable due to the incohesive quality of the core material (not suitable for core measurements) and core loss in the highly fractured parts of the borehole.

Porosity is first derived from GPR velocities using the so-called Complex Refractive Index Method (CRIM), which requires a representative dielectric constant of the rock matrix  $\epsilon$ . The porosity estimate is then subsequently converted into density using a grain density typical for granitic formations. To constrain the transformations, an upper and lower dielectric constant is chosen iteratively so that lab densities from competent samples fall between the resulting calculated density logs (GPR dens  $\epsilon=5.8$  and  $\epsilon=6.2$ ). The support volume of the BHR data is around 2 m, and thus, smoothens out the strong fluctuations due to intense fracturing observed in the other well logs. To obtain a porosity and density log on a smaller scale the NN measurement is utilized. For this, the NN log is calibrated with the GPR porosity in the intact formation (NN GPR por), or porosity lab measurements (NN Lab por), both leading to similar estimates. The calculated porosity logs are then subsequently converted into density logs (NN GPR dens, NN Lab dens). The resistivity log, which samples different support volumes of the formation depending on the chosen spacing, could not be converted into porosity due to the strong influence of surface conductivity, which overrides the response due to open fracture porosity.



## Acknowledgements

This work was supported by the Swiss National Science Foundation through the National Research Programme 70 “Energy Turnaround” and completed within the Swiss Competence Center on Energy Research - Supply of Electricity (SCCER-SoE), with the support of the Swiss Commission for Technology and Innovation. We thank Yannick Forth and Jörg Renner from the Ruhr-University Bochum for Archimedes-type density measurements.

# Attenuation in fluid-saturated fractured porous media: quasi-static numerical upscaling vs dynamic wave propagation modeling

Eva Caspari<sup>1</sup>, Mikhail Novikov<sup>2</sup>, Vadim Lisitsa<sup>2</sup>, Beatriz Quintal<sup>1</sup>, Nicolas Barbosa<sup>1</sup>, J. Germán Rubino<sup>3</sup> and Klaus Holliger<sup>1</sup>  
<sup>1</sup>University of Lausanne, Switzerland, <sup>2</sup>Institute of Petroleum Geology and Geophysics, Novosibirsk, Russia, <sup>3</sup>CONICET, Centro Atómico Bariloche – CNEA, Argentina

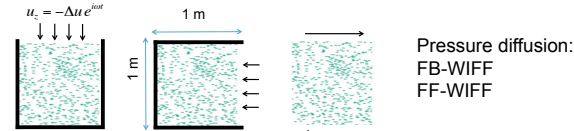
## 1. Motivation

Fractures are of great interest in earth sciences and in civil engineering since they significantly influence the elastic and hydraulic properties of geological formations. Seismic attributes are commonly used to detect and characterise fracture zones. One such attribute which recently gained increased attention is seismic attenuation. However, several mechanisms can cause wave attenuation and velocity dispersion in fluid-saturated fractured porous media comprising, on the one hand, pressure diffusion phenomena, such as fracture-to-background (FB) and fracture-to-fracture (FF) wave-induced flow (WIFF), and, on the other hand, dynamic effects, such as scattering and Biot global flow. In this study, we compare attenuation estimates from wave propagation simulations with corresponding estimates from a numerical upscaling approach. The former captures all aforementioned attenuation mechanisms and their interplay, though detailed interpretations tend to be difficult. The latter only accounts for pressure diffusion phenomena and thus will be guiding the physical interpretation. Understanding the interplay of attenuation mechanisms is an essential first step for estimating petrophysical properties from seismic measurements.

## 2. Numerical methods

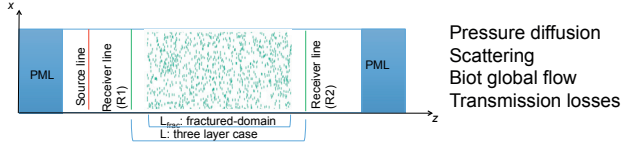
### Numerical upscaling based on Biot's quasi-static equations (QS)

Oscillatory compression and shear tests (Rubino et al. 2016):



### Wave propagation transmission based on Biot's dynamic equations (WP)

Transmission experiment (Novikov et al. 2017, Masson et al. 2006):

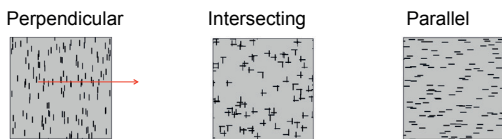


Domain size: 2 - 5 wavelengths (20 correlation lengths of the medium)

## 3. Fractured medium

Background: stiff porous matrix

Fractures: compliant porous inclusions with a width of 4 mm and a length of 30 mm



### Attenuation mechanisms

Perpendicular	Intersecting	Parallel
Scattering	Scattering	Scattering
FB WIFF	FF WIFF	
Biot global flow (B+F)	Biot global flow (F)	Biot global flow (F)

### Permeability

	Host	Fracture
Perpendicular	$10^{-10} \text{ m}^2 - 10^{-17} \text{ m}^2$	$10^{-9} \text{ m}^2$
Intersecting	$10^{-17} \text{ m}^2$	$10^{-9} \text{ m}^2 - 10^{-14} \text{ m}^2$
Parallel	$10^{-17} \text{ m}^2$	$10^{-8} \text{ m}^2 - 10^{-14} \text{ m}^2$

### References:

Masson, YJ, SR Pride, & KT Nihei, 2006. Finite difference modeling of Biot's poroelastic equations at seismic frequencies, *Journal of Geophysical Research: Solid Earth*, 111 (B10).  
Novikov, M., E. Caspari, V. Lisitsa, B. Quintal, J. G. Rubino & K. Holliger, 2017. Attenuation in fluid-saturated fractured porous media— Quasi static numerical upscaling and wave propagation modeling: In proceedings of the 6th Biot Conference on Poromechanics, pp. 1499-1506  
Rubino, J.G., E. Caspari, T.M. Müller, M. Milani, N. Barbosa & K. Holliger, 2016. Numerical upscaling in 2-D heterogeneous poroelastic rocks: Anisotropic attenuation and dispersion of seismic waves, *Journal of Geophysical Research: Solid Earth*, 121 (9), 6698-6721.

## 4. Modeling results

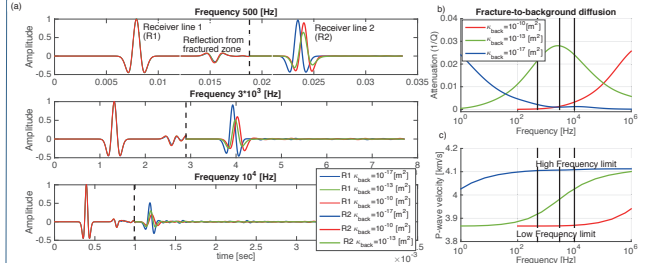


Figure 1: Example for the perpendicular case a) Transmission experiment: Recorded averaged waveforms at receiver line 1 and 2 for three central frequencies and permeabilities. The black dashed line separates the two recordings. b) Resulting P-wave attenuation and c) phase velocity as function of frequency from the oscillatory tests. The black lines correspond to the central frequencies of the signals shown in a).

## 5. Attenuation and velocity estimation

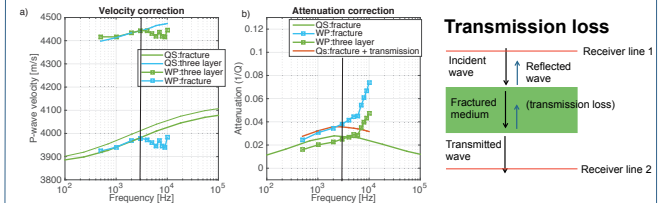


Figure 2: a) Effective velocities of the fractured domain and the three layer case for the transmission experiment (WP) and oscillatory test (QS). The black line indicates the onset of scattering. b) Attenuation estimate for the fractured domain and the three layer case.

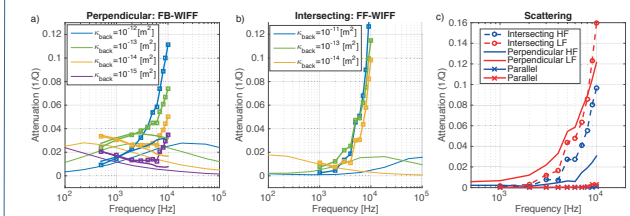


Figure 3: Attenuation comparison for a) perpendicular case (FB-WIFF) and b) intersecting case (FF-WIFF) and c) scattering in the low- and high-frequency limits for all three types of the fractured medium.

## 6. Conclusions

To interpret wave propagation results in terms of intrinsic attenuation caused by a fractured medium, we have to account for the travel path of the wave and amplitude reductions due to transmission losses. After correcting for these effects the good agreement between the transmission experiment and oscillatory test, indicates that, at low frequencies pressure diffusion phenomena are dominant, whereas at higher frequencies scattering attenuation starts to control the response. The magnitude of scattering attenuation varies considerably depending on the arrangement of fractures and the effective compliance of the fractured medium, which in turn is strongly influenced by the pressure diffusion phenomena.

**Acknowledgements:** This work has been completed within the Swiss Competence Center on Energy Research - Supply of Electricity, with the support of the Swiss Commission for Technology and Innovation. V. Lisitsa and M. Novikov are thankful to the Russian Foundation for Basic Research grants no. 16-05-00800, 17-05-00250, 17-05-00579 for financial support of the research. Simulations of seismic wave propagation were performed on clusters of the Siberian Supercomputer Center.

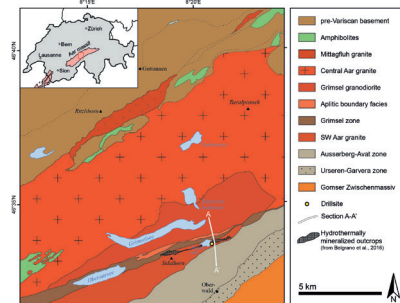
# Fault structure and porosity distribution in an active hydrothermal system

Daniel Egli<sup>1</sup>, Rahel Baumann<sup>1</sup>, Sulamith Küng<sup>1</sup>, Alfons Berger<sup>1</sup>, Ludovic Baron<sup>2</sup> & Marco Herwegh<sup>1</sup>

<sup>1</sup>Institute of Geological Sciences, University of Bern (daniel.egli@geo.unibe.ch), <sup>2</sup>Institut des sciences de la Terre, Université de Lausanne

## Motivation and approach

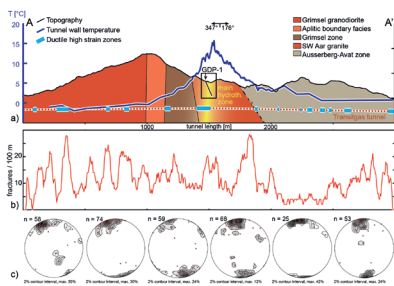
The geometry of fracture networks and matrix porosity of fault rocks are key parameters controlling the permeability and ultimately the fluid flux along fault zones. On the example of a long-lived and still active fault-bound hydrothermal system (Grimsel breccia fault; Hoffmann et al., 2004; Belgrano et al., 2016) in the crystalline basement of the Aar Massif (Swiss Alps), this study aims at understanding the extent, occurrence, dynamics and evolution of natural fluid pathways along faults and their characteristics in hydrothermal zones in particular. Better understanding of such naturally porous and permeable rocks is of prime importance for the successful exploration of natural hydrothermal systems. On the basis of structural data collected from an inclined 125 m long drillhole, the corresponding drill core and surface mapping, we evaluate the porosity, permeability and fracture distribution around a central water-bearing breccia zone from the micrometre to decametre scale and its significance for past and present fluid circulation.



Geologic map of the central Aar massif, modified after Berger et al., (2016).

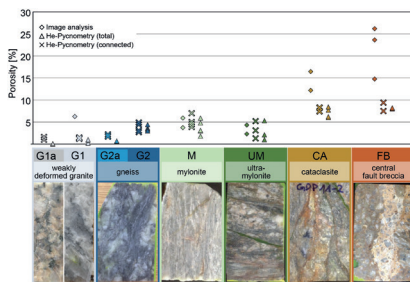
## Large-scale temperature distribution and fractures

a) Geologic cross-section along the Transitgas AG tunnel below Grimsel Pass showing the drillhole (projected into section), rock-wall temperatures and main ductile high strain zones, b) Elevated fracture density along the cross-section correlates with ductile high strain zones, but only one of these zones shows hydrothermal inflow. c) Lower hemisphere equal-area pole plots of mapped fractures reflect the regional ENE-WSW main structural trend.



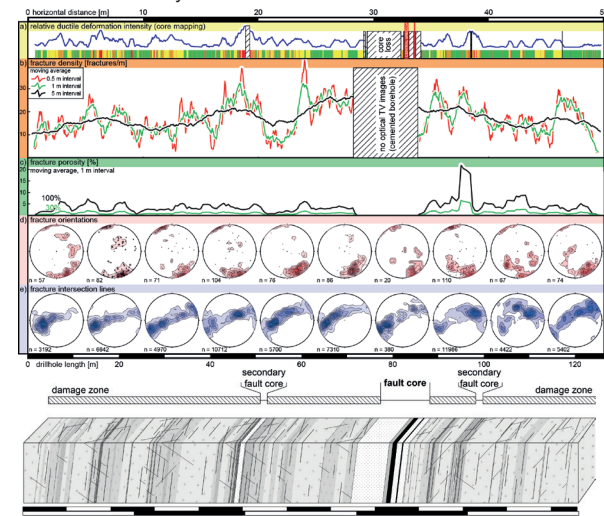
## Matrix porosity measurements

Porosity data from the matrix- and microfracture-porosity measurements show a correlation between deformation intensity and matrix porosity ranging from <1vol% to >20vol%. Comparable to the macroscopic fractures, the micro-porosity is strongly controlled by the intensity of precursory deformation. Fault core rock analyses yield highly elevated matrix porosity.



## Meso-scale fracture distribution

The main fracture orientation is controlled by a regional ENE-WSW trend forming sub-parallel high-strain zones interconnected by NW-SE trending fracture sets. There is a strong correlation between ductile deformation intensity and fracture density/porosity. Increased fracture density and high fracture volume suggest two secondary fault cores north and south of the central fracture zone. Clusters of intersection lines might represent a network of focused linear flow-paths along the main trend of the hydrothermal zone.



Schematic block-diagram of the examined deformation zone indicating the variable and alternating grade of ductile deformation, the observed fracture pattern as well as the central fault core and secondary fault cores.

## Discussion

Fracturing is controlled by regularly spaced variations in ductile deformation intensity ranging from granite to ultramyylonite. The variable degree of ductile precursory deformation shows a range of matrix porosity values between <0.1 and 7% and thus forms a succession of subparallel sealing and high-porosity structures bridged by a dense fracture network. Fluid flow is therefore directly related to the combined effect of fractures and enhanced fault-related matrix porosity. In this specific setting, the width of the damage zone exceeds the distance between the large scale faults that can be observed on the surface and which are characterized by a regular increase in fracture density. However, of several such parallel fault zones, the Grimsel breccia fault is the only one showing enhanced heat flow. This suggests a key importance of matrix porosity within fault core rocks (breccia & fault gouge) for the transport of hydrothermal fluids as an enhanced fracture network alone is not providing sufficient permeability in the case of this natural hydrothermal system.

## Acknowledgments

This project is part of the NRP70 program and is funded by the Swiss National Science Foundation. We thank Swisstopo, the Swiss Federal Office of Energy, NAGRA and the Kraftwerke Oberhasli AG for additional financial and practical support.

## References

Belgrano, T.M., Herwegh, M. & Berger, A. 2016: Inherited structural controls on fault geometry, architecture and hydrothermal activity: an example from Grimsel Pass, Switzerland. *Swiss Journal of Geosciences*.  
Berger, A., I. Mercogli, and E. Gnos 2016: Geological map of the Aar Massif, Tavetsch and Gotthard nappes 1:100000, *Landesgeologie der Schweiz*.  
Hoffmann, B.A., Helfer, M., Diamond, L.W., Villa, I.M., Frei, R. & Eikenberg, J. 2004: Topography-driven hydrothermal breccia mineralization of Pliocene age at Grimsel Pass, Aar massif, Central Swiss Alps. *Schweiz. Mineral. Petrogr. Mitt.*, 84, 271–302.

# Characterization and imaging of a fractured crystalline hydrothermal fault zone from hydrophone VSP data

A. Greenwood, E. Caspari, J. Hunziker, L. Baron, and K. Holliger.

In cooperation with the CTI

Energy  
Swiss Competence Centers for Energy Research

Schweizerische Eidgenossenschaft  
Confédération suisse  
Confederazione Svizzera  
Confederaziun svizra  
Swiss Confederation

Commission for Technology and Innovation CTI

70 NRP  
Energy Turnaround  
National Research Programme

## Borehole hydrophones for fracture characterisation

Petrothermal reservoirs with sufficient potential for electric power generation prevail at depths between 4-6 km. At these depths, current drilling techniques return limited rock samples for fracture and fluid pathway analysis. Thus, there is a large dependence on borehole geophysical techniques to determine the fracture characteristics, hydraulic properties and the extent of targets drilled. Borehole hydrophones record pressure waves originating from seismic body-waves passing the borehole. However, due to the high sensitivity of hydrophones and their suspension in the fluid column, they are susceptible to strong

coherent noise trapped within the water column known as tube-waves. Tube-waves are generated at large impedance contrasts in the borehole wall such as open fractures. As such, hydrophones are well suited to identify and characterise hydraulically open fractures and to map deformation zones. For these reasons, we analyse hydrophone-based vertical seismic profiling (VSP) experiments along the GDP1 borehole, which penetrates the Grimsel Breccia Fault (GBF) as well as the embedding fractured granitic rocks. The GBF has been exhumed to a depth of 3-4 km and is considered to exhibit pertinent analogies to a deep fractured petrothermal target.

### Tube-waves

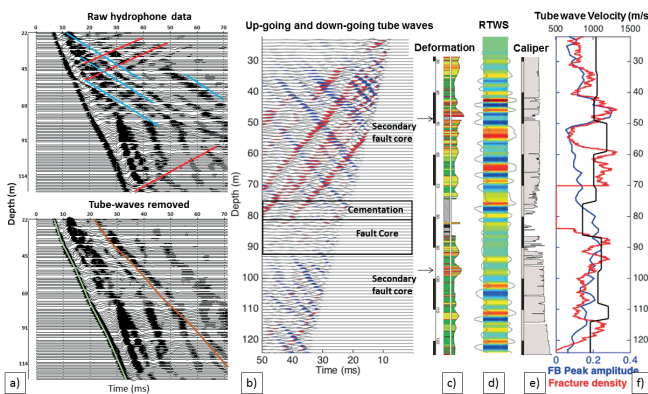


**Figure 1** (a) Zero-offset VSP data before (top) and after (bottom) up- and down-going tube-wave (red and blue lines, respectively) removal through *f-k* filtering, (b) superposition of up- and down-going tube-waves extracted from the data shown in (a), (c) relative deformation intensity log from core analysis, (d) reflected tube-wave stack (RTWS), (e) calliper log, and (f) first-arrival amplitudes (blue), fracture density from televiwer data (red) and tube-wave velocity (black). The black box denotes the main fault core and black arrows identify two secondary fault cores.

### Seismic imaging

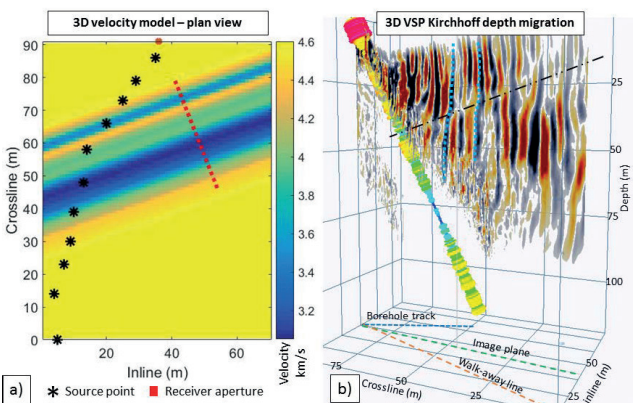


**Figure 2** (a) Plan view of the 3D velocity model derived from smoothed zero-offset VSP interval velocities, surface projection of walk-away sources and extent of hydrophone string, and (b) pre-stack depth migration (PSDM) image taken on a plane bisecting the borehole plane and walk-away VSP source line. Neutron-neutron data is displayed along the borehole track identifying the main fault core (blue) and upper secondary fault (green), which is bisected by a sub-horizontal structural lineation (dashed black line). Reflections from the top and bottom of the main fault core are indicated by blue dashed lines.

### Channel waves

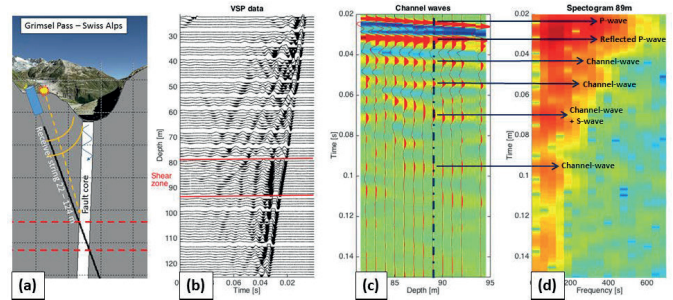


**Figure 3** (a) Simplified cross-section of the GBF showing the deeply incised topography, the geometry of the borehole intersecting the main fault core, the location of the seismic source and borehole hydrophone receivers and a schematic of channel waves generated within the GBF due to its high impedance contrast with regard to its embedding environment. (b) Zero-offset hydrophone VSP data with the GBF main fault core highlighted by the red rectangle. (c) Seismic traces from the main fault core (red rectangle). (d) Dispersion analysis of the seismic trace at depth 89 m indicated by the dashed line in (c). Identified within the spectrogram are the first arriving P-wave, the strongly reflected P-wave, later arriving channel waves and a channel wave overlapped by a down-going S-wave. Note the decrease in channel wave frequency with time.

### Conclusions and outlook

The Grimsel breccia fault, as well as its embedding fractured crystalline environment, have been characterized using hydrophone VSP and well log data. Fractures indicating brittle deformation are accurately mapped by the reflected tube-wave stack (Figure 1d). This is also supported by the presence of unusually high amplitudes of the first arrivals at the fracture locations (Figure 1f). In addition, the main fault core similarly causes high-amplitude first-arrivals. However, there is an absence of observable tube-waves within the fault core due to borehole breakouts, which inhibit tube-wave propagation and thus uniquely identifies the main deformation zone (Figure 1b).

The generation of a laterally changing 3D velocity model from zero-offset VSP interval velocities and the implementation of 3D pre-stack depth migration, necessitated by out-of-plane source points, has been successful in seismically imaging the near-vertical fault structures (Figure 2) and a potential, as of yet unknown, sub-horizontal structure, which bisects the borehole coincidentally at the upper secondary fault core.

The creation of channel waves requires a large impedance contrast to the surrounding formation, such as a breccia embedded in crystalline rock. Thus, the identification of these wavefields clearly identifies the GBF core, whilst the decrease of frequency observed in Figure 3 is indicative of geometrical dispersion. The modelling and analysis of dispersion to further characterize the GBF is an avenue of future work, as is the determination of the shear modulus from tube-wave velocities and the modelling of fracture properties from tube-waves (Poster Hunziker et al).

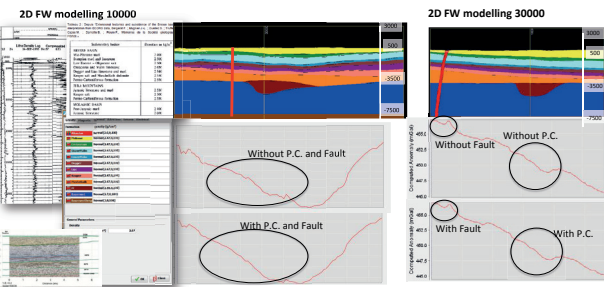
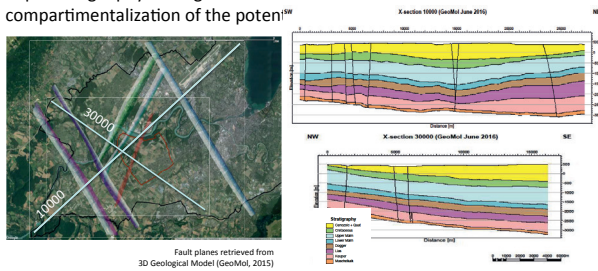
**Acknowledgements** We thank: Daniel Egli, from the University of Bern for structural deformation and fracture density measurements and Yannick Forth and Jörg Renner from the Ruhr-University Bochum for Archimedes-type density measurements. This work was supported by the Swiss National Science Foundation through the National Research Programme 70 "Energy Turnaround" and completed within the Swiss Competence Center on Energy Research - Supply of Electricity (SCCER-SoE), with the support of the Swiss Commission for Technology and Innovation.

# Gravity survey in the Geneva Basin for deep geothermal and heat storage projects

Luca Guglielmetti<sup>1</sup>, Goran Mijic<sup>1</sup>, Andrea Moscarello<sup>1</sup>, David Dupuy<sup>2</sup>, Piervittorio Radogna<sup>2</sup>  
<sup>1</sup>Earth Science Department, University of Geneva; <sup>2</sup>Geo2X SA

**Abstract:** A gravity survey has been carried out in the Geneva area with the goal to collect new high resolution data in three main areas on interest for the geothermal development in Geneva. 1227 new stations have been collected in the Bernex, Thonex and Allondon area. The approach is to produce 3D density models for the study sites and integrate them to the existing geophysical data (2D seismic, VSP and CSEM) to develop integrated models produced by the joint interpretation of the different datasets to reduce the exploration risk of future geothermal projects.

**Design:** The acquisition has been designed taking into account the results of the forward gravity modelling of the the 3D geological model from GeoMol which provided some geometrical constraints of the different formations at depth. Density values were retrieved by different data sources. Particular attention has been devoted to the presence of faults which could have an important geophysical signature and that could affect the compartmentalization of the poten<sup>ti</sup>

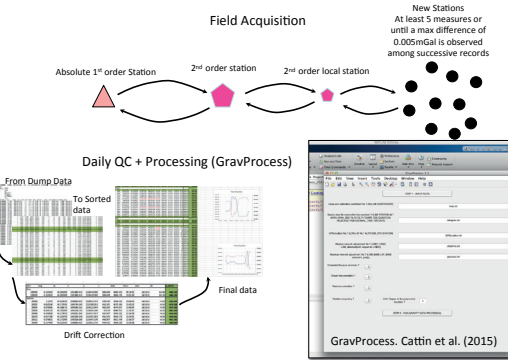
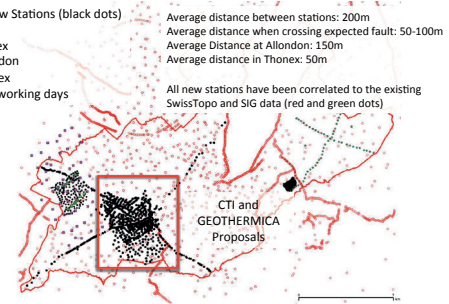


## Acquisition

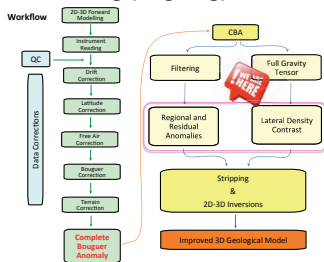
1227 New Stations (black dots)  
3 Areas:  
• Bernex  
• Allondon  
• Thonex  
52 field working days

Average distance between stations: 200m  
Average distance when crossing expected fault: 50-100m  
Average Distance at Allondon: 150m  
Average distance in Thonex: 50m

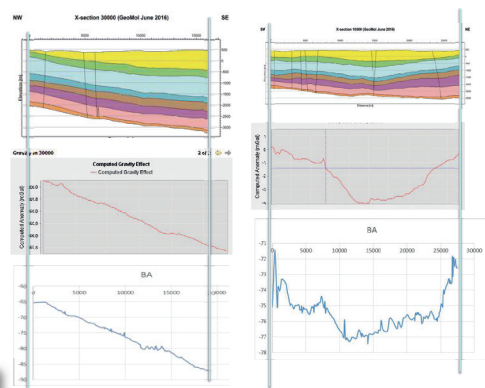
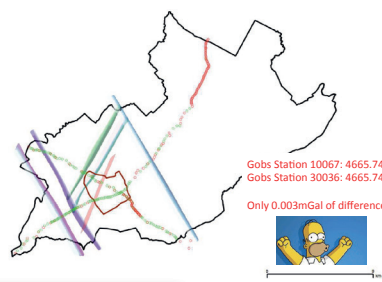
All new stations have been correlated to the existing SwissTopo and SIG data (red and green dots)



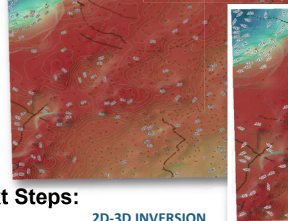
## Processing (ongoing):



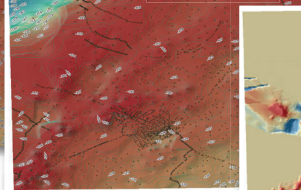
## Good quality data



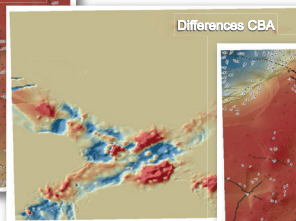
CBA Before the Survey



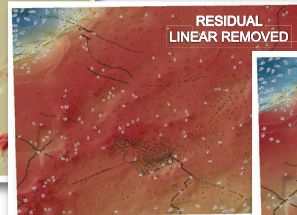
CBA After the Survey



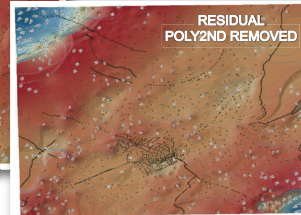
Differences CBA



RESIDUAL LINEAR REMOVED



RESIDUAL POLY2ND REMOVED



## Next Steps:

2D-3D INVERSION

STRIPPING

GRAVITY TENSORS

KEEP ON PROCESSING!!!

# VSP survey at the Thonex Well - Geneva

L. Guglielmetti<sup>1</sup>, A. Moscariello<sup>1</sup>, M. Francois<sup>2</sup>, C. Nawratil de Bono<sup>2</sup>, C. Dezayes<sup>3</sup>, B. Adnand<sup>3</sup>, P. Corubolo<sup>4</sup>, F. Poletto<sup>4</sup>  
<sup>1</sup>Earth Science Department, University of Geneva; <sup>2</sup>Services Industriels de Geneve; <sup>3</sup>BRGM; <sup>4</sup>INOGS Trieste

**Abstract:** In the framework of the Geothermie 2020 program and the FP7 IMAGE project a VS survey has been carried out in the Thonex geothermal well in 2016. The main goals were:

- Acquire a detailed velocity model to improve the GeoMol 3D Model
- Characterize the carbonate formations
- Highlight fault zones
- Develop an acquisition approach which can be applied for further wells

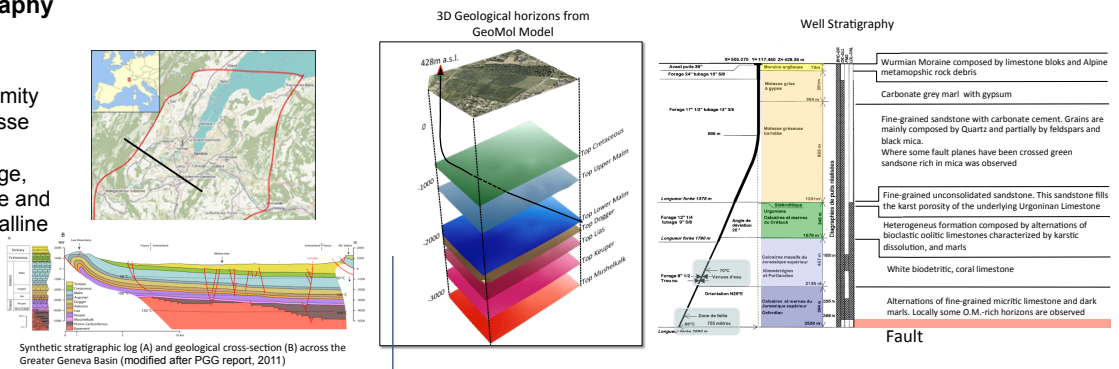
The collected data show an overall good quality and helped constraining the velocity model of the main potential geothermal reservoirs and highlight some anisotropies in the Molasse sediments which can reflect a layered structure of the deposits.

## The Thonex Geothermal Well

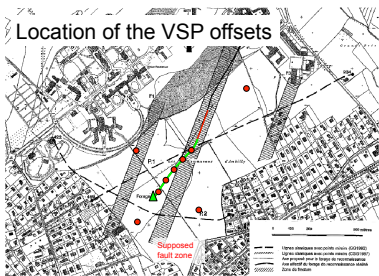
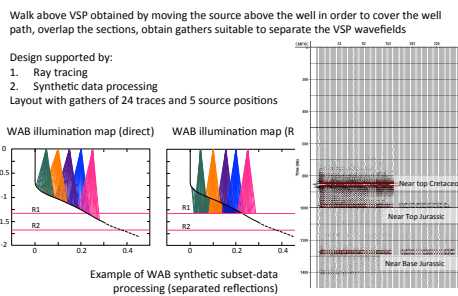
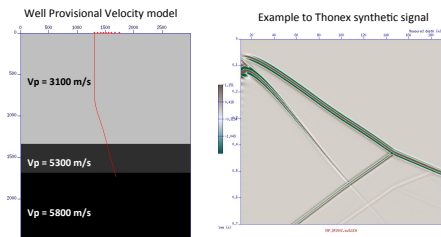
- The Thonex well was drilled in 1993 with the goal to tap a deep thermal aquifers in the Jurassic formations to provide heat for district heating.
- A TVD of 2530m was reached with a deviated geometry towards NE (MD 2690m)
- Ground water was tapped in the Upper Jurassic reef limestones, but at rates below expectations.
- Well testing via air lift indicated a stabilized flowrate of 11 m<sup>3</sup>/h, originating from Upper Jurassic limestones at a depth of about 1900 m and a fluid temperature of 70°C as evidenced by production logging. The geothermal gradient, measured at 3.12°C/100
- The well is now accessible only down to 1500m MD

## Local Geology and Stratigraphy

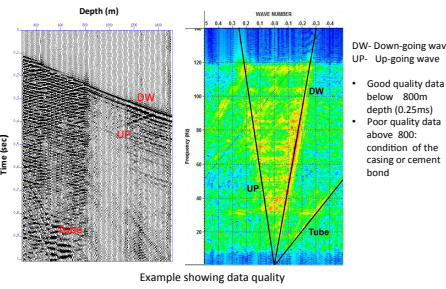
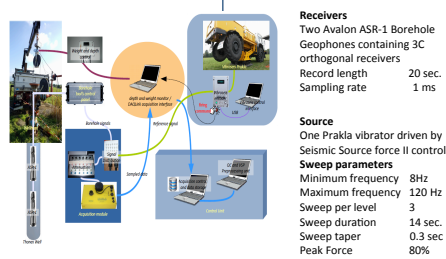
The Greater Geneva region is a Swiss-French transnational zone located at the southwestern extremity of the North Alpine foreland Molasse basin. It consists of a thick sedimentary cover of Mesozoic age, principally composed of carbonate and marl formations, overlying a crystalline basement often incised by depressions filled with Permo-Carboniferous sediments.



## Design



## Acquisition and Field QC

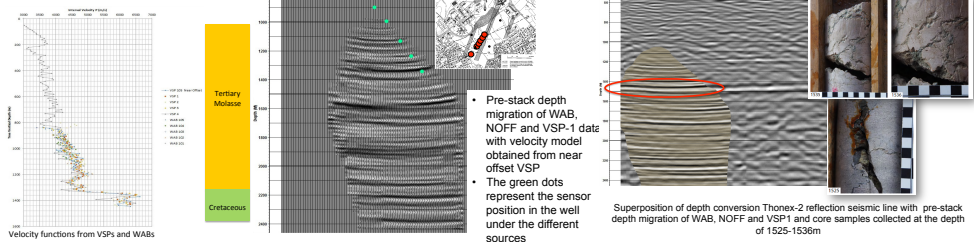


## Processing

Main processing steps:

- Header adjustment
- Source receiver offset calculation
- Frequency analysis
- Band-pass filtering (8-12-110-120 Hz)
- First Break (FB) picking
- Velocity analysis
- Wavefield separation
  - Mean scaling in 20ms window centered on the FB
  - Median filter (7 traces)
  - FK filter design
  - FK filter for upgoing enhancement
  - Two Way Time (TWT) with and without NMO verticalization
  - Predictive deconvolution
  - Wave shaping deconvolution
  - Spherical divergence recovering
  - Corridor mute and corridor stack
- Kirchhoff migration

## Results



## Conclusions:

- Overall good quality data even though some noisy signal in the upper 700m due to casing is observed
- Good coherence between offsets velocity models
- Some important reflections on the WAB are observed at 1500 (Karst), 1800, 2100 and 2300m strongly improving the resolution of vintage 2D seismic lines

# Seismic attenuation in porous rocks containing stochastic fracture networks

Jürg Hunziker\*, Marco Favino\*, Eva Caspari\*, Beatriz Quintal\*, J. Germán Rubino<sup>§</sup>, Rolf Krause<sup>°</sup> and Klaus Holliger\*  
 \*Université de Lausanne, Switzerland // <sup>°</sup>Università della Svizzera italiana, Switzerland // <sup>§</sup>CONICET Centro Atómico Bariloche, Argentina

## Introduction

Direct imaging of fractures with seismic waves is generally not possible as the seismic wavelengths tend to be much larger than the aperture of the fractures. To overcome this limitation, we study the attenuation of seismic waves in fractured rocks due to fluid pressure diffusion (FPD) with the goal to use the attenuation, expressed as the inverse of the quality factor  $1/Q$ , to characterize fracture networks. To this end, we perform numerical upscaling experiments on 2D rock samples featuring stochastic fracture networks. Fractured samples are simulated as poroelastic media. We apply compression and shear tests (Rubino et al., 2009) based on Biot's quasi-static poroelastic equations (Biot, 1941) to obtain P- and S-wave attenuation, respectively.

## Fracture Model

A fractured sample is generated by drawing the fracture length from a distribution similar to the one of de Dreuzy et al. (2001):

$$n(l, L) = d_c L^2 (a - 1) \frac{l^{-a}}{l_{min}^{-a+1}} \text{ for } l \in [l_{min}, l_{max}]$$

The fracture thickness is kept constant at 0.5 mm and the length of the sample  $L$  is 0.4 m. The fracture length is varying between  $l_{min} = 0.01$  m and  $l_{max} = 0.2$  m. Instead of the fracture density  $d_c$ , which defines the amount of fracture center points per unit area, we use the fracture density  $d_a$ , which defines how much area of the sample is covered by fractures. We simulate different samples by changing the fracture density  $d_a$  and the characteristic exponent  $a$ :

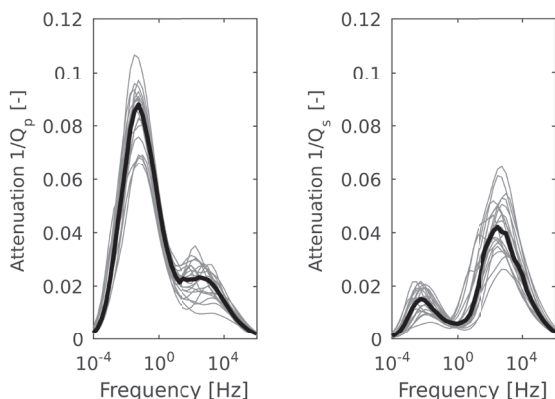
**a = 1.5;  $d_a = 1.5\%$**     **a = 3;  $d_a = 1.5\%$**     **a = 3;  $d_a = 3\%$**



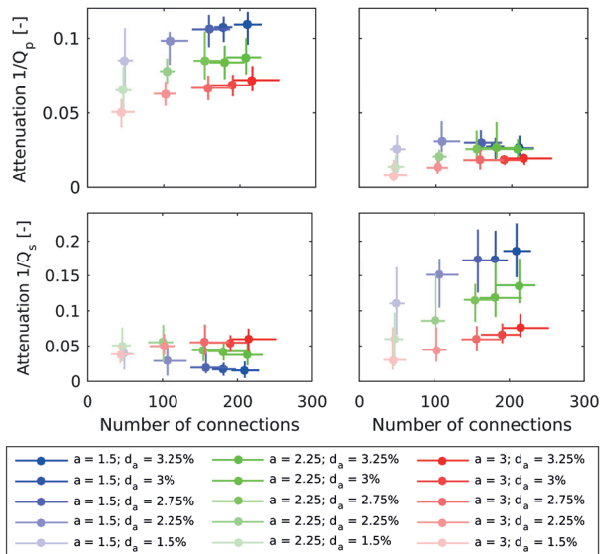
The characteristic exponent  $a$  controls the appearance of long fractures relative to short ones. A small value of  $a$  represents a distribution with more long fractures, whereas a large  $a$  represents a distribution with only very few long fractures. Fractures are considered to be connected if they overlap at least partially.

## Results

After having carried out the compression and the shear tests at different frequencies, we obtain the P- and S-wave attenuation due to FPD. For each combination of  $a$  and  $d_a$ , we generate 20 different samples. The attenuation for the 20 samples generated for  $a = 1.5$  and  $d_a = 1.5\%$  is shown below with gray curves. The bold black curve is the median of these 20 attenuation curves.



The low-frequency attenuation peak corresponds to FPD from the fracture into the background, while the high-frequency peak is due to FPD within connected fractures (Rubino et al., 2013). We observe, that for P-waves the fracture-to-background process is dominant, while for S-waves the fracture-to-fracture process is more important. Executing these two tests for five different fracture densities  $d_a$ , three different values of the characteristic exponent  $a$ , 20 different samples for each combination and 41 different frequencies, results in 24'600 simulations. We have summarized all these information by plotting the mean and the range of the magnitude of the two attenuation peaks as a function of fracture connections:



We observe, that the attenuation changes with the amount of fracture connections. Thus, seismic attenuation due to FPD is sensitive to the local connectivity. However, global connectivity, i.e. the presence of a fully connected fluid path, is more difficult to detect. For a detailed interpretation of the data see Hunziker et al. (2017).

## Conclusions and Outlook

Our numerical experiments indicate that seismic attenuation due to fluid pressure diffusion is sensitive to the local connectivity of the fractures. Information about the global connectivity is more difficult to extract.

In the future, we aim to investigate the attenuation behavior of anisotropic fracture networks and simulations in 3D. We also aim to study a combination of seismic and resistivity measurements in order to obtain more detailed connectivity information.

## References

Biot, M. A. (1941), General theory for three-dimensional consolidation, *Journal of Applied Physics*, 12, 155–164.  
 de Dreuzy, J.-R., P. Davy, and O. Bour (2001), Hydraulic properties of two-dimensional random fracture networks following a power law length distribution: 1. Effective connectivity, *Water Resources Research*, 37, 2065–2078.  
 Hunziker, J., Favino, M., Caspari, E., Quintal, B., Rubino, J. G., Krause, R., and Holliger, K. (2017), Seismic attenuation and modulus dispersion in porous rocks containing stochastic fracture networks, *Journal of Geophysical Research*, under revision.  
 Rubino, J. G., C. L. Ravazzoli, and J. E. Santos (2009), Equivalent viscoelastic solids for heterogeneous fluid-saturated porous rocks, *Geophysics*, 74, N1–N13.  
 Rubino, J. G., L. Guarracino, T. M. Müller, and K. Holliger (2013), Do seismic waves sense fracture connectivity?, *Geophysical Research Letters*, 40, 692–696.

# Towards fracture characterization using tube waves

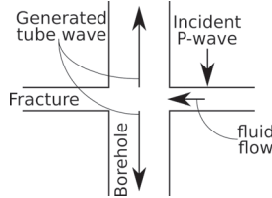
Jürg Hunziker\*, Shohei Minato<sup>o</sup>, Eva Caspari\*, Andrew Greenwood\* and Klaus Holliger\*  
\*Universität de Lausanne, Switzerland // <sup>o</sup>Technische Universiteit Delft, The Netherlands

## Introduction

Tube waves are generated and reflected at intersections between a borehole and one or more fractures. Their amplitude depends notably on the fracture compliance and the hydraulic transmissivity of the fracture. Therefore, tube waves have significant potential for characterizing fractures in terms of their mechanical and hydraulic properties. The main ingredient of a corresponding inversion algorithm is an accurate and efficient solver of the forward problem. For this purpose, we test the analytical tube wave model described by Minato and Ghose (2017).

## Tube wave generation

When a P-wave hits a fracture intersecting a borehole, the fracture is compressed. This induces fluid flow from the fracture into the borehole, which in turn generates a tube wave in the borehole.



Minato and Ghose (2017) describe the generation of a tube wave due to this mechanism with the tube wave potential  $\Phi_g$

$$\phi_g(z) = \sum_{i=1}^N \frac{2}{\rho_f c_T} \frac{p_i^{(i)}}{p_{inc}^{(i)}} \delta(z - z_i),$$

where  $N$  is the number of fractures in the medium,  $\rho_f$  the density of the fluid,  $c_T$  the speed of the tube wave and  $\delta$  the Dirac function.

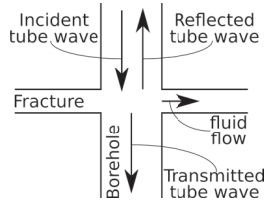
Depth is denoted by  $z$  and the sub- or superscripts  $i$  give the properties of the  $i$ th fracture. The pressure fields of the tube wave  $p_i$  and the incoming P-wave  $p_{inc}$  are given by

$$p_i^{(i)}(\omega) = \sigma_0 \frac{j\omega c_T \rho_f Z \alpha_{eff} H_1(\zeta R)}{k_r \alpha_f R H_0(\zeta R)} \quad \text{and} \quad p_{inc}^{(i)}(\omega) = \sigma_0 \frac{\rho_f c_T^2}{\rho V_S^2} \left( \frac{1 - 2V_S^2/V_P^2}{1 - c_T^2/V_P^2} \right),$$

where  $\sigma_0$  is the amplitude of the normally incident plane P-wave,  $\omega$  the angular frequency,  $k_r$  the radial wavenumber in the rigid, non-deformable fracture,  $\alpha_f$  the fluid velocity,  $Z$  the fracture compliance,  $\alpha_{eff}$  the effective fluid velocity in the fracture (including the fracture compliance), and  $R$  the borehole radius.  $H_n$  denotes the Hankel function of the first kind and order  $n$  and  $\zeta$  the effective radial wavenumber.

## Tube wave scattering

When a tube wave propagating through a borehole encounters a fracture, fluid flow from the borehole into the fracture is triggered. This leads to reflection and transmission of tube waves.



Minato and Ghose (2017) describe this with the scattering potential  $\Phi_s$

$$\phi_s(z) = j\omega \sum_{i=1}^N \eta^{(i)} \delta(z - z_i),$$

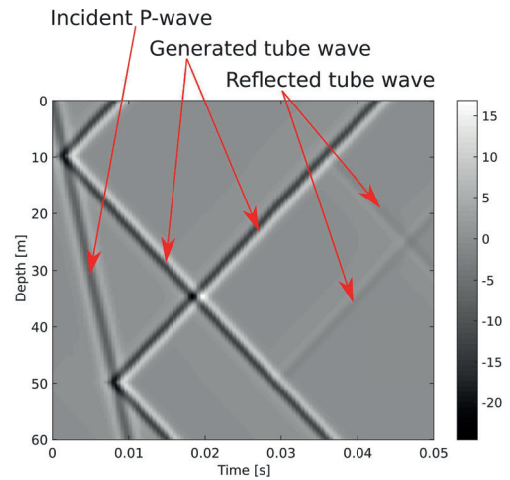
where  $j$  is the imaginary unit and  $\eta$  the interface compliance given by

$$\eta = -\frac{2\zeta}{R} \frac{L_0}{k_r^2 \alpha_f^2 \rho_f} \frac{H_1(\zeta R)}{H_0(\zeta R)},$$

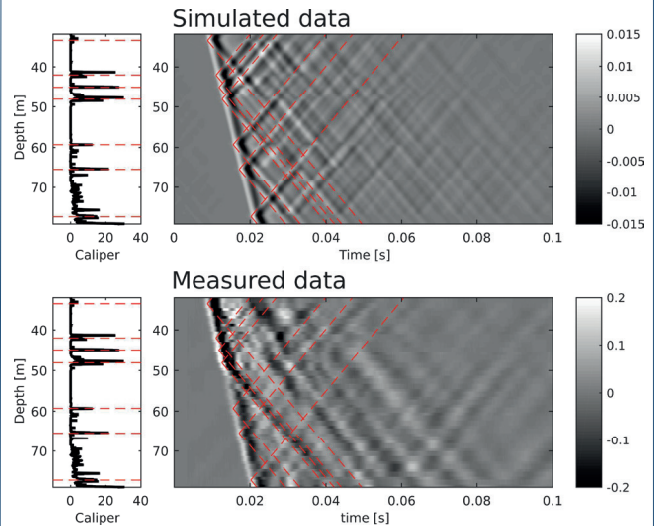
with  $L_0$  denoting the fracture aperture.

## Results

We start by considering a simple model with two identical fractures with an aperture  $L_0$  of 2 mm.



Next, we consider a more realistic model of a fractured rock mass based on evidence from the GDP1 borehole on the Grimsel Pass. The locations of the fractures are inferred from the caliper log while their mechanical and hydraulic properties are chosen to be uniform. Despite these simplifications, the overall resemblance between the observed and simulated tube wave records is remarkably close, which in turn indicates that the problem might be amenable to a global inversion approach.



## Conclusions

We have implemented a new method for tube wave modeling and applied it to a simplified model of the fractured crystalline rocks penetrated by the GDP1 borehole on the Grimsel Pass. The results are encouraging and indicate that the inversion of tube wave data might allow for the characterization of fractures in terms of their mechanical and hydraulic properties.

## Reference

Minato, S. and R. Ghose (2017), Low-frequency guided waves in a fluid-filled borehole: Simultaneous effects of generation and scattering due to multiple fractures, *Journal of Applied Physics*, 121, 104902.

## Importance of dolomitization of the Upper Jurassic carbonate rocks for geothermal prospection in the Geneva Basin (Switzerland & France)

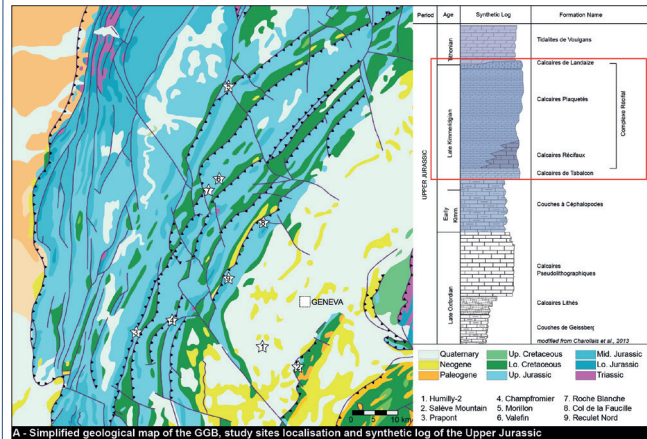
Makhloufi Y.\*, Rusillon E.\*, Brentini M.\*, Meyer, M., Samankassou E.\*  
(yasin.makhloufi@unige.ch)



### Introduction and geological context

The Canton of Geneva is currently exploring the opportunities for geothermal energy exploitation in the Geneva Basin (GB) sub-surface. It has been shown that the Upper Jurassic, and more particularly the Kimmeridgian limestones, are affected by dolomitization processes (e.g. Charollais, 1996, 2013; Deville, 1988; Fookes, 1995; Meyer, 2000; Mouchet, 1998; Rameil, 2008; Strasser, 2015). Such diagenetic processes are often associated with important modifications in the reservoir properties of the rock by poro-genesis or poro-necrosis mechanisms. Dolomitized limestones already proved to be productive reservoir for geothermal exploitation in time-equivalent deposits in South-Germany.

Based on field analogues and sub-surface data (Fig. A), our main objectives are: (1) to provide a detailed diagenetic history of the Kimmeridgian units in the GB, (2) to discuss the origin of the dolomitization processes when encountered and finally, (3) to propose a diagenetic model to allow our results to be used during further exploration of the basin and compared with petrophysical characterization of the reservoir units.



A - Simplified geological map of the GGB, study sites localisation and synthetic log of the Upper Jurassic

### Methods

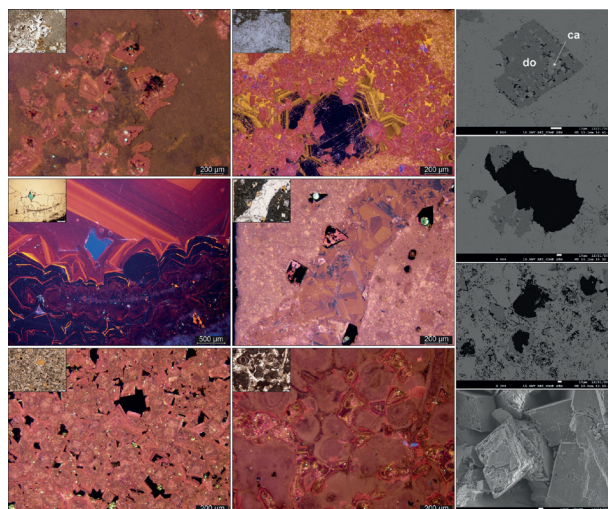
- Samples from outcrops and cores were prepared for thin section analysis. Thin sections, impregnated with epoxy resin dyed by Methylene blue, were used to define the texture, grain type, cement type, and pore-type distribution.
- Sequence of diagenetic events and their mineralogy was constrained using Cathodoluminescence (CL) analysis and Calcite staining.
- S.E.M. images and semi-quantitative analyses and mapping helped further characterization of diagenetic features.

### Results

Most of the initial porosity in the different unit studied was filled by the precipitation of several stages of calcite cementations.

**Dolomitization** precipitated during early diagenesis and overprinted any precedent stages. In most of the case, the dolomitization is mainly represented by planar, replacement dolomite.

**Dedolomitization** is observed a by either: (1) an almost complete dissolution leading to the creation of secondary pore space or (2) a two-step calcitization driven by the infiltration of Ca-rich water leading to dissolution, formation of microvugs and then precipitation of calcite.



### Major Insights

The Upper Jurassic carbonate rocks form a complex carbonate reservoir strongly affected by diagenesis. Based on the petrographic data acquired from sub-surface and outcrops, the following conclusions can be made:

- Dolomitization occurred during early diagenesis and overprinted all precedent stages. The most affected units are the Calcaires de Tabacon and the Calcaires Récifaux.
- The first stages of dolomitization are interpreted to be induced by a reflux-type model involving mesosaline to hypersaline fluid originating from evaporitic conditions in a lagoonal environment. The third stage of replacive, fabric-destructive dolomite is explained by shallow burial dolomitization producing syntaxial overgrowth dolomite over pre-existing nuclei. **This process is responsible for the highly porous sucrosic dolomite occurring in the Reculet section.**
- Dedolomitization is identified at different order of magnitude by either: (1) an almost complete dissolution leading to the creation of secondary pore space or (2) a two-step calcitization driven by the infiltration of Ca-rich water leading to dissolution, formation of micro-vugs and then precipitation of calcite.
- **The creation of secondary pore space could provide a good connectivity between the intraparticulate or matricial microporous network and the interparticulate moldic macroporous network. This enhanced connectivity could therefore provide good reservoir properties suitable for geothermal energy exploitation.**

Carbonate heterogeneities remains to be a major issue when assessing the exploitation potential. Understanding of the paragenesis affecting such reservoirs is an important step towards a better exploitation of resources currently available.

### Conclusions and Outlooks

- ✓ New insights on the diagenesis that affected the GB and associated fluid migrations.
- ✓ Understanding of how the pore network evolved can be used to explain the reservoir properties observed in the Upper Jurassic carbonate rocks of the GB.



- **Objectives:** assessment of geothermal potential in the Geneva Basin carbonate rocks
- **Concept:** characterization of diagenetic features, pore network and impact on reservoir properties
- **Main Partners:** Services Industriels Genevois (SIG), Etate de Genève (GESDEC), University of Geneva

# Investigation of the evolution in physical properties of crustal rocks with different degree of microfracturation.



Lucas Pimienta & Marie Violay  
Laboratory of Experimental Rock Mechanics, EPFL, Lausanne, Switzerland



### Motivation:

Field seismic and electrical resistivity are powerful tools to investigate from the surface geological reservoir rocks at depth.

The two methods are complementary and have been largely used to prospect for oil/gas reservoirs. However, little is still known on the intrinsic dependences of the two properties to the degree of microfracturation (e.g. Pimienta et al., 2017). Moreover, electrical properties have seldom been measured in the high pressure and high temperature range (Violay et al., 2012)

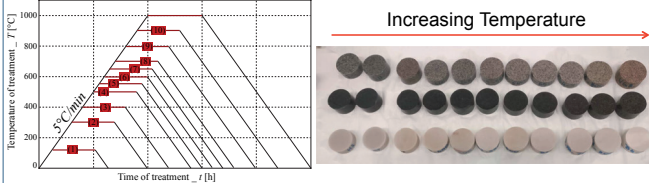
Using thermal treatment at different temperatures, known to induce a variable degree of microfracturation in rocks (e.g. Nasser et al., 2007), the aim of this work is to investigate how the degree of microfracturation affects the physical properties of rocks.

### Project:

- **PROGRESS**: PROspection and PROduction of Geothermal REServoirS
- Understand the links between physical properties in geothermal reservoir rocks.

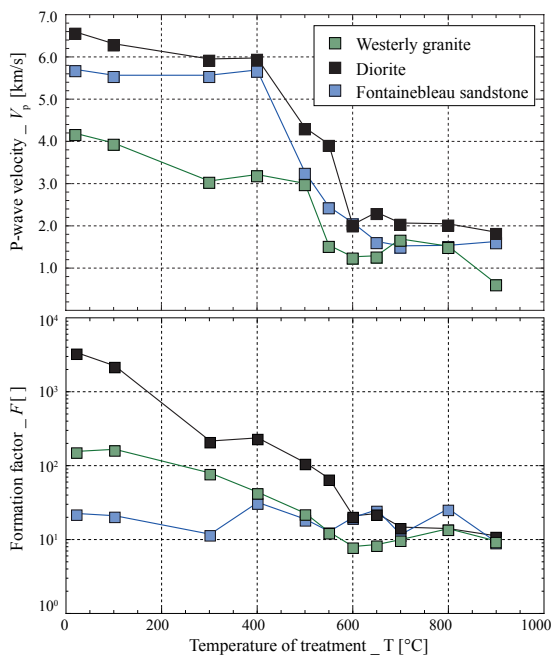
### Samples & Methods:

- Approach: Evolution in properties for varying degree of damage
- ➔ Thermal treatment in oven for T in the range of [20,1000] °C



- Rocks samples: (11 for each rock)
  - **Diorite**:  $\phi = [0.1; 0.3]\%$  // Approx. 30 % quartz
  - **Granite** (Westerly):  $\phi = [0.7; 1.3]\%$  // Approx. 30 % quartz
  - **Sandstone** (Fontainebleau):  $\phi = [4.1; 6.4]\%$  // Quartz of 100%
- Petrophysical characterisation:
  - Porosity
  - P- & S-wave velocities
  - Electrical impedance:
    - Frequency of 1 kHz
    - Pore fluid : Brine (tap water + 1g/L of NaCl)

### Results

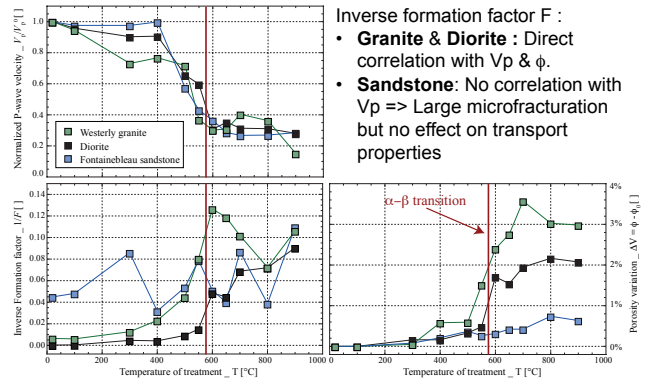


Variable dependence to the temperature for the two properties & the different rock types:

- Elastic properties: Large decrease in Vp starting from 400°C, for all rocks
- Electrical properties:
  - Largest decrease for the **Diorite** (T < 600°C)
  - Largest decrease for the **Granite** (T < 600°C)
  - No variation for **Sandstone**

### Interpretation

- Normalised Vp : Same variations for all rocks. Decrease of up to about 80% of the initial property  
=> Very large degree of damage for all three samples.
- Inverse formation factor F :  
=> **Granite & Diorite** : Variations for same T as Vp.  
=> **Sandstone**: Large microfracturation but no effect on F or  $\phi$ .



### Conclusion

- Dramatic effects of the temperature in rocks, even though temperature rate is kept low
  - ⇔ Role of grains anisotropic thermal expansions.
- Variable dependence to the temperature for the different properties, and the different rocks.
- Rather than being the trigger of changes in properties, the  $\alpha$ - $\beta$  transition is the temperature for which the properties reach their asymptotic value.
  - ⇔ The transition may not be the cause for the variations in properties !?
- Independent of the thermal variation, large effects of the rock type:
  - **Diorite**: not initially microcracked & not porous => Most dramatic effects on all properties
  - **Granite**: Initially microcracked & not porous => Less dramatic effects but same variations for all properties
  - **Sandstone**: not initially microcracked, but porous => Dramatic effects still observed for Vp, but little change in porosity and permeability.

### References

- Nasser, M. H. B., Schubnel, A., & Young, R. P. (2007). Coupled evolutions of fracture toughness and elastic wave velocities at high crack density in thermally treated Westerly granite. *International journal of rock mechanics and mining sciences*, 44(4), 601-616.
- Pimienta L., Sarout, J., Esteban, L., David, C., & Clennell, B. (2017): Pressure-dependent Elastic, Electric and Hydraulic transport properties of porous and permeable rocks: Insights into the links between transport properties. *Journal of Geophysical Research*, **major revisions**.
- Violay, M., Gibert, B., Azais, P., Pezard, P. A., & Lods, G., 2012. A new cell for electrical conductivity measurement on saturated samples at upper crust conditions. *Transport in porous media*, 91(1), 303-318.

# A numerical approach for studying attenuation in interconnected fractures

Beatriz Quintal<sup>1</sup>, Eva Caspari<sup>1</sup>, Klaus Holliger<sup>1</sup>, and Holger Steeb<sup>2</sup>  
<sup>1</sup>University of Lausanne, Switzerland; <sup>2</sup>University of Stuttgart, Germany

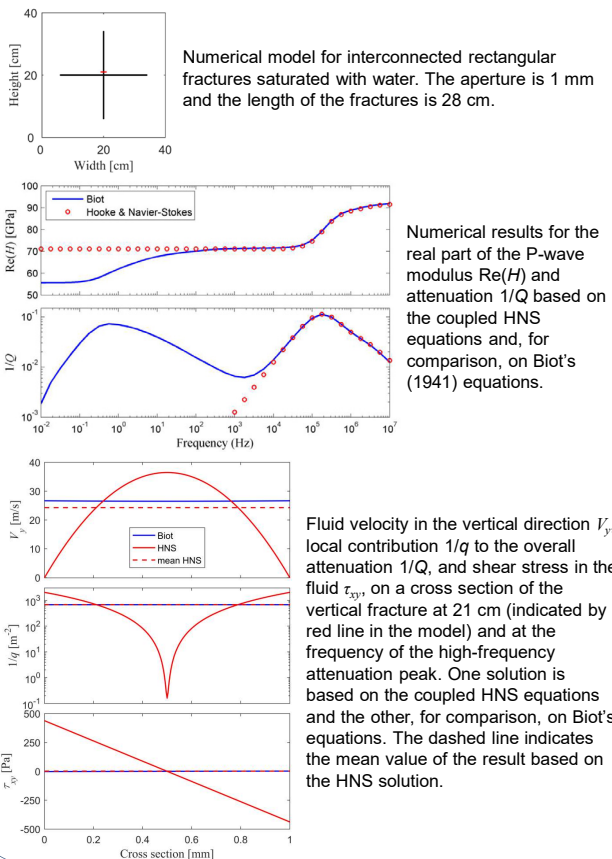
## Introduction

Squirt flow is the main cause of acoustic dissipation in porous rocks fully saturated with a liquid. Classical microscopic models for squirt flow are based on interconnected microcracks (O'Connell and Budiansky, 1977) or on microcracks connected to spherical pores (Murphy et al., 1986). A squirt-type flow may, however, also occur at the mesoscopic scale within hydraulically interconnected fractures. This phenomenon is thus a potential indicator of fracture interconnectivity and was numerically studied by Rubino et al. (2013) using Biot's (1941) equations to describe both fractures and background as porous and permeable media. Vinci et al. (2014) then used a scheme that couples Biot's equations to describe the porous and permeable background with a 1D solution of Navier-Stokes equations for fluid flow within the fractures. Here we propose a simpler approach that couples Hooke's law with the Navier-Stokes (HNS) equations to describe the laminar flow of a viscous compressible fluid in conduits that are embedded in an isotropic, linear elastic solid.

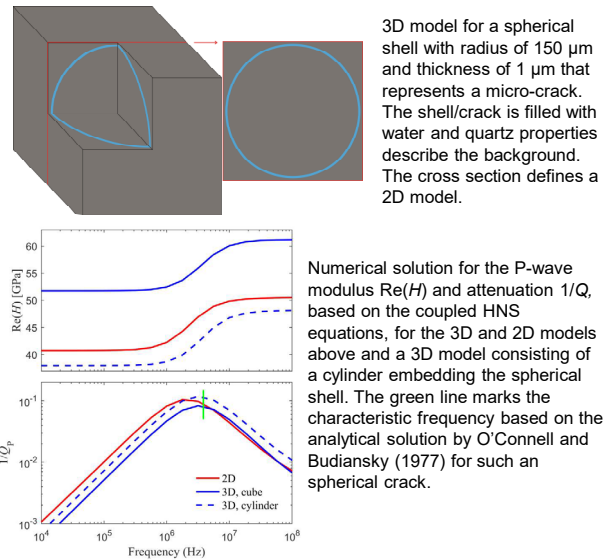
## Numerical scheme

The coupled HNS equations reduce to Hooke's law in the subdomains representing an elastic solid and to the linearized, quasi-static Navier-Stokes' equations in the subdomains representing a compressible viscous fluid by simply accordingly setting the values of three material parameters throughout the numerical model: shear viscosity, and bulk and shear moduli (Quintal et al., 2016). The equations are solved in the frequency domain and the results allow for the dissipation caused by fluid flow or, more accurately, by fluid pressure diffusion.

## Results compared to those based on Biot's equations



## Results compared to an analytical solution for squirt flow



## Conclusions and outlook

Numerical results based on the coupled Hooke and Navier-Stokes (HNS) equations were compared with those based on Biot's equations for a scenario involving interconnected fractures. We observed excellent agreement of results for the overall attenuation caused by squirt-type flow, despite differences in the attenuation spatial patterns. At much lower frequencies, the results differ because pressure diffusion in the porous background, described by Biot's equations, is not accounted for by the coupled HNS equations.

Attenuation was also computed based on the coupled HNS equations for a 3D model involving a spherical crack. The frequency of the attenuation peak was successfully compared with that from an analytical solution for squirt flow, which further validates our approach.

Our numerical analyses show that the proposed scheme based on the coupled HNS equations can be readily employed to study flow in interconnected mesoscopic fractures as well as the microscopic squirt flow. In the coming years, we will derive 3D models from micro-tomography images of thermally fractured glass samples to compute frequency-dependent attenuation. The results will then be compared with laboratory measurements of seismic attenuation in those fractured samples. This follow-up research will be co-funded by the Swiss National Science Foundation (SNSF) and the German Research Foundation (DFG) in the context of a recently approved cross-border research project.

## References

Biot (1941) General theory of three-dimensional consolidation: Journal of Applied Physics  
 Murphy, Winkler, and Kleinberg (1986) Acoustic relaxation in sedimentary rocks, dependence on grain contacts and fluid saturation: Geophysics  
 O'Connell and Budiansky (1977) Viscoelastic properties of fluid-saturated cracked solids: Journal of Geophysical Research - Solid Earth  
 Quintal, Rubino, Caspari, and Holliger (2016) A simple hydromechanical approach for simulating squirt-type flow: Geophysics  
 Rubino, Guarracino, Müller, and Holliger (2013) Do seismic waves sense fracture connectivity?: Geophysical Research Letters  
 Vinci, Renner, and Steeb (2014) On attenuation of seismic waves associated with flow in fractures: Geophysical Research Letters

# Quantification of the 3D thermal anomaly in the orogenic geothermal system at Grimsel Pass

Christoph Wanner, Larryn W. Diamond, Peter Alt-Epping,  
Institute of Geological Sciences, University of Bern (wanner@geo.unibe.ch)

## Motivation

Orogenic belts without active igneous activity are recognized as plays for geothermal power production. Owing to lower discharge temperatures than those in volcanic-regions, these systems, which we refer to as "orogenic geothermal systems", are classified as low-enthalpy resources. In the framework of the SCCER-SoE Task 1.1 we are conducting thermal hydraulic (TH) modeling of the orogenic geothermal system at Grimsel Pass to quantify its 3D geothermal anomaly and to evaluate the general potential of such orogenic geothermal systems for geothermal power production.

## The Grimsel Pass geothermal system

- Discharge of hydrothermal springs with  $T \leq 28^\circ\text{C}$  into a gas tunnel beneath Grimsel Pass
- They occur over a narrow tunnel section of <100 m, where it intersects the WSW-ENE-striking Grimsel Breccia Fault (GBF)
- Hydrothermal activity is also manifested by the occurrence of a 3 Ma old hydrothermal breccia formed ~3 km below the paleosurface
- Oxygen isotopes and fluid inclusions in quartz and adularia reveal a meteoric fluid origin and a breccia formation temperature of  $165^\circ\text{C}$
- The Na-K geothermometer applied to the thermal spring waters provides strong evidence that the circulating meteoric water reaches a temperature of at least  $214^\circ\text{C}$ , and more likely  $\sim 250^\circ\text{C}$
- Such temperatures correspond to a remarkable penetration depth of ~10 km, given that the background geothermal gradient of  $25^\circ\text{C}/\text{km}$  is the only source of heat in the area.

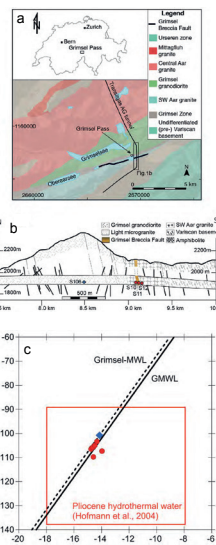


Fig. 1: (a,b) Geological map and cross section of the Grimsel Pass area showing the localities of thermal (red symbols) and cold springs (blue symbol). (c)  $\delta^2\text{H}$  vs.  $\delta^{18}\text{O}$  of cold and thermal springs indicating their meteoric origin. (d) Ternary Na-Kg-Mg Gigenbach diagram demonstrating that all thermal spring samples (filled circles) plot on the  $214^\circ\text{C}$  isotherm.

## Model setup

- Simulation of the upflowing segment only
- Large 3D domain to capture the interplay between advective and conductive heat transport
- Constant width of the GBF along the tunnel (100 m)
- Variable extent of the upflow zone parallel to the GBF (50–150 m)
- Initial hydrostatic pressure distribution
- $P > P_{\text{hydrostatic}}$  below upflow zone, corresponding to the hydraulic head driving the system (500–800 m)
- Initial conductive temperature distribution

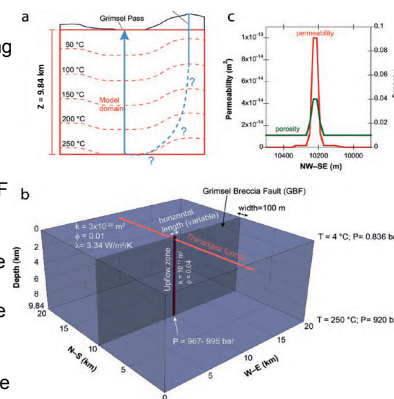


Fig. 2: (a) Schematic meteoric water circulation model. (b) Model setup with specified initial and boundary conditions. (c) Specified permeability and porosity profile along the Transitgas tunnel.

## Sensitivity analysis

- Steady-state temperature distribution is approached in less than 5000 a
- Model results demonstrate that the extent of temperature anomalies induced by fracture-flow hydrothermal systems is mainly controlled by
  - the 3D extent of the fault system
  - the upflow velocity, i.e., by the fault zone permeability as well as the hydraulic head gradient driving hydrothermal circulation

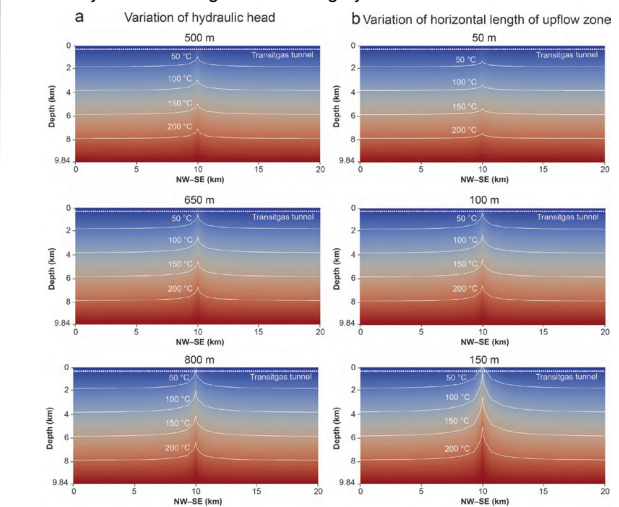


Fig. 3: Simulated steady-state temperature distributions for various combinations of hydraulic head differentials and horizontal length of the upflow zone parallel to the GBF. The panels show the model slice that is perpendicular to the GBF and that includes the Transitgas tunnel.

## Quantification of the thermal anomaly

- The model was calibrated against the discharge temperature of thermal springs and the temperature recorded along the tunnel wall
- Breccia formation temperature and  $T_{\text{discharge}}$  could not be matched with the same parameter set, suggesting that the upflow rate was larger when the hydrothermal breccia was formed 3 Ma ago
- The calibrated model was used to calculate the heat in excess of that provided by the background conductive temperature profile:

$$H = \sum_i C_p \cdot \rho \cdot V_i \cdot \Delta T_i$$

$C_p$ : heat capacity;  $\rho$ : bulk rock density;  $V_i$ : volume of grid block  $i$ ;  $\Delta T_i$ : difference to background  $T$  profile

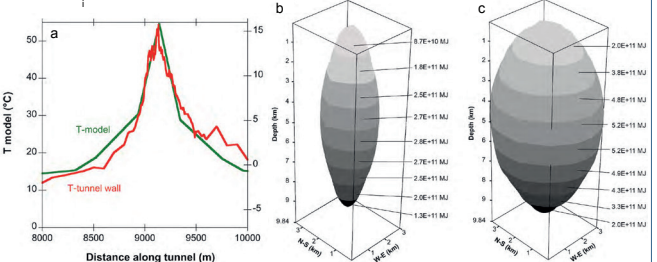


Fig. 4 (a): Comparison between measured and modeled temperatures along the wall of the Transitgas tunnel. (b, c) Anomalous heat per km depth predicted for: (b) the calibrated model simulating the current flow system and (c) the model simulating the temperature of the fossil system (i.e.,  $165^\circ\text{C}$  at a depth of ~3 km).

## Conclusions

- Converting heat excesses shown in Figures 4a,b to theoretical geothermal power output by dividing by time (20 a) yields values from 10–40 MW per km depth, demonstrating that orogenic geothermal systems are promising plays for geothermal power production
- Based on our modelling, exploration should focus on high topography areas such as those in the Vallais and in surrounding valleys of the Central Alps where hydraulic head gradients and hence upflow rates are at maximum values.

# Causes of abundant calcite scaling in geothermal wells in the Bavarian Molasses Basin, Southern Germany

Christoph Wanner<sup>1</sup>, Florian Eichinger<sup>2</sup>, Thomas Jahrfeld<sup>3</sup>, Larry W. Diamond<sup>1</sup>

<sup>1</sup>Institute of Geological Sciences, University of Bern (wanner@geo.unibe.ch); <sup>2</sup>Hydroisotop GmbH, Schweitenkirchen, Germany;

<sup>3</sup>Reneco Plan Consult, Munich, Germany

## Motivation

Over the past 15 years the Bavarian Molasse Basin in southern Germany has become a veritable hotspot for geothermal power. Currently 22 geothermal power plants are being operated. Typical flow rates are between 30 and 130 L/s and the production temperatures reach up to 150 °C. Despite these favorable reservoir conditions, the use of many of the wells for heat and power production is highly challenging. The main difficulty, especially in the deep (>3000 m) boreholes with temperatures >120°C, is that substantial calcite scaling is hindering the proper operation of the pumps within the wells and of the heat exchangers at the surface. As a consequence, high maintenance costs (e.g., replacing downhole pumps: ~€500'000) still inhibit the economically sustainable operation of these plants. For this study, we used a combination of analytical and numerical techniques to identify the main processes controlling calcite scaling at the Kirchstockach geothermal plant, located 15 km SE of Munich.

## Kirchstockach geothermal power plant

- Binary cycle power plant with an installed capacity of 5.5 MW<sub>el</sub>
- Downhole pump is installed at 800 m depth
- Scale formation is observed at the pump, the riser pipe and in the plant at the surface
- Scales consist of almost pure calcite with minor corrosion products (magnetite, pyrrhotite, pyrite)
- Scaling thicknesses correspond to a low calcite precipitation rate of about  $1.2 \times 10^{-9}$  mol/s/m<sup>2</sup>

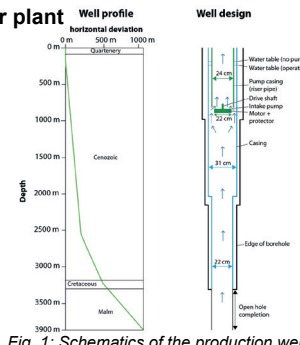


Fig. 2: Scales formed along (a) the pump, (b) the riser pipe, and (c) in installations of the geothermal plant at the surface.

## Wellhead water samples

- Weakly mineralized Na-HCO<sub>3</sub>- water type (TDS: 430-500 mg/L)
- Constant production temperature of 135°C
- Constant composition with respect to major anions and cations
- Varying composition with respect to dissolved [Ca<sup>2+</sup>] and [HCO<sub>3</sub><sup>-</sup>]
- reflects varying calcite saturation state
- Calcite and dolomite dissolution rates are rather fast

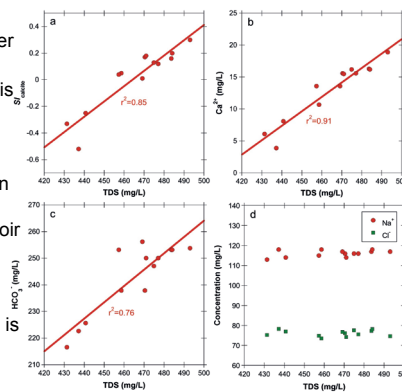


Fig. 3: Variation in compositions of wellhead fluid samples. SI: saturation index. TDS: total dissolved solids.

- Chemical equilibrium is likely to prevail under in-situ reservoir conditions
- Well head composition does not reflect the composition at reservoir P,T
- Variation in TDS and deviation from carbonate equilibrium is an effect of scaling formation
- Carbonate equilibrium (SI=0) is obtained by numerically adding CO<sub>2</sub>

## Fluid inclusions

- Gas (N<sub>2</sub>+CO<sub>2</sub>) and petroleum inclusions are identified in calcite crystals
- Demonstrate the presence of a free gas phase in the upflowing water + petroleum (3-phase system)
- Dissolved gas concentrations of wellhead samples are well below saturation (at T=135°C, 18 bar)
- Homogenization temperature of petroleum inclusions T<sub>h</sub> correspond to the production temperature (T<sub>h</sub>=128–138 °C; T<sub>prod</sub>=135°C)
- No indication of an unwanted temperature increase in the well

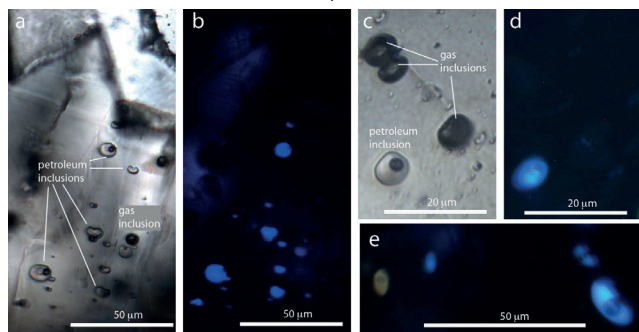


Fig. 4: Examples of primary gas and petroleum inclusions observed in calcite crystals. Microphotographs (a) and (c) taken under normal transmitted light. Microphotographs (b), (d) and (e) taken under UV reflected light.

## Preferred scaling formation model

All observations can be explained by the following sequence of processes:

- Carbonate equilibrium is prevailed at reservoir conditions (SI=0)
- Pressure somewhere drops to 4-6 bar within the production well
- Owing to its local pressure minimum, the pump is the most likely location
- Effect of the fast rotating centrifugal pump (i.e. cavitation, Fig. 6)
- Boiling of the produced fluid
- N<sub>2</sub> and CO<sub>2</sub> are stripped into gas phase
- Immediate calcite supersaturation (SI<sub>calcite</sub>>>0)
- Gas phase partially persists
- Scaling formation during further upflow and in the power plant
- Trapping of gas (CO<sub>2</sub>, N<sub>2</sub>) in precipitating calcite crystals

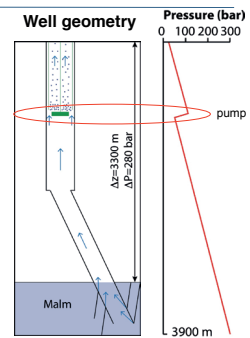


Fig. 5: Boiling scenario and idealized pressure profile along the well.



Fig. 6: Cavitating propeller model in a water tunnel experiment.

	P (bar)	Water composition				Gas composition					
		HCO <sub>3</sub> (mg/L)	CO <sub>2</sub> (mg/L)	N <sub>2</sub> (NmL/kg)	pH	SI <sub>calcite</sub>	Sg (vol%)	H <sub>2</sub> O (vol%)	N <sub>2</sub> (vol%)	CO <sub>2</sub> (vol%)	(N <sub>2</sub> /CO <sub>2</sub> ) (vol ratio)
Simulation	4.6	241	132	10.1	6.69	0.35	8.4	73.2	19.4	7.4	2.6
Sample KST-12	-	241	132	8.0	6.67	0.30	-	-	-	-	2.37-6.9

Table 1: Comparison of measured wellhead fluid composition with that predicted from boiling calculations (CHILLER). Also shown is the simulated N<sub>2</sub>/CO<sub>2</sub> ratio of the coexisting gas phase in comparison to the ratio measured in gas inclusions.



## For more information:

Causes of abundant calcite scaling in geothermal wells in the Bavarian Molasse Basin, Southern Germany

Christoph Wanner<sup>1</sup>, Florian Eichinger<sup>2</sup>, Thomas Jahrfeld<sup>3</sup>, Larry W. Diamond<sup>1</sup>

<sup>1</sup> Institut für Geoökologie, Institut für Geoökologie, Universität Bern, Bernstrasse 31, CH-3012 Bern, Switzerland

<sup>2</sup> Hydroisotop GmbH, Wolfstrasse 8, D-82031 Schweitenkirchen, Germany

<sup>3</sup> Reneco Plan Consult GmbH, Giesingstrasse 46, D-80333 München, Germany

# Measuring pressure dependent fracture aperture distribution in rough walled fractures using X-ray computed tomography

Quinn C. Wenning and Claudio Madonna – Department of Earth Sciences, ETH Zurich  
Lisa Joss and Ronny Pini – Department of Chemical Engineering Imperial College London

## 1. Introduction

- Knowledge of fracture (aperture) distribution is paramount for sound description of fluid transport in low-permeability rocks.
- In the context of geothermal energy development, quantifying the transport properties of fractures is needed to quantify the rate of heat transfer and optimize the engineering design of the operation.
- Core-flooding experiments coupled with non-invasive imaging techniques (e.g., X-Ray Computed Tomography – X-Ray CT) represent a powerful tool for making direct observations of these properties under representative geologic conditions.

## 2. Sample preparation and characterization

- Thermally treated samples (cycles of heating to 400 °C followed by quenching) with slightly enhanced porosity (1.6 % heat treated vs. 0.7 % no treatment) were prepared with a diameter = 5 cm and length = 10 cm.
- A single fracture along the core was induced via a modified Brazilian test with pointed wedged spacers placed along the top and bottom of the sample.



Fig. 1 Left: Brazilian induced fracture and Right: comparison of thermally shocked (left) and not shocked (right) samples.

## 3. Computed tomography methods

- The method for fracture aperture estimation follows the calibration free missing attenuation method [Huo et al., 2016].
- CT number in the vicinity of a fracture will be reduced due to density deficiency in the gas filled fracture.
- Smearing of the X-ray attenuation due to partial volume effects will cause lower CT numbers adjacent to the fracture.
- Main assumption is that all X-ray attenuation is conserved and that the real CT value of the un-fractured rock can be estimated by neighboring voxels.

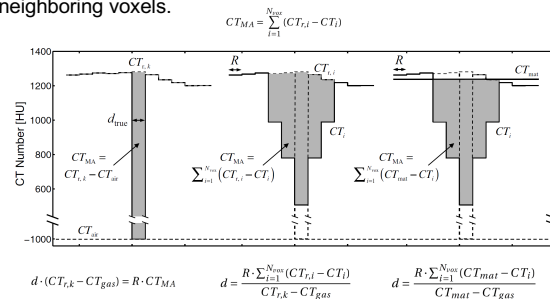
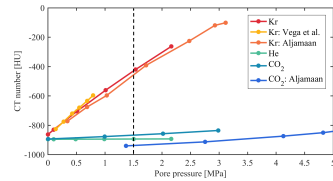


Fig. 2 Schematic of true fracture, smeared fracture with estimated matrix CT [Huo et al., 2016].

Fig. 3 The use of He and Kr gases with differing CT number allows us to estimate fracture aperture with two fluids independently.



## 4. Results

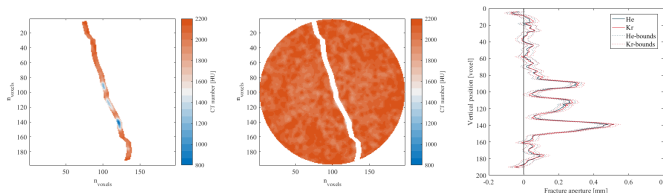


Fig. 4 CT scans of the fracture trace (left) and matrix area (middle), and aperture estimation using He and Kr (right) for a single slice.

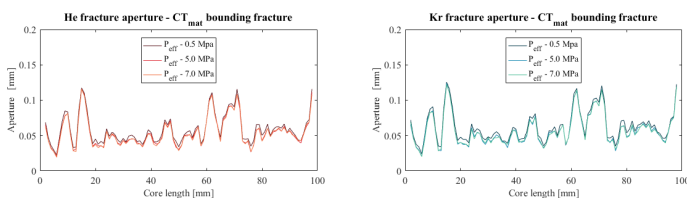


Fig. 5 1D average hydraulic aperture along the length of the core for increasing effective pressure (i.e., average aperture per slice scan).

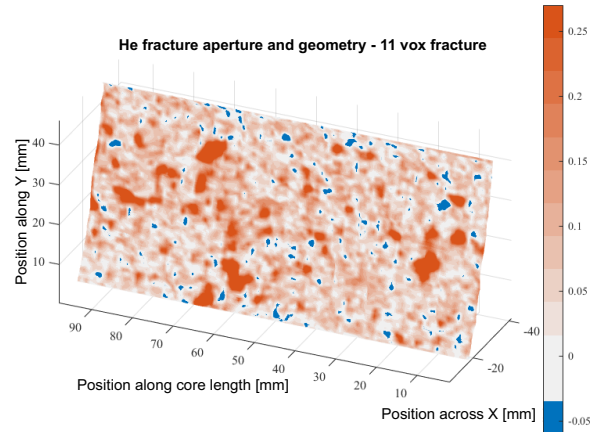


Fig. 6 Fracture aperture heterogeneity for a 5 MPa effective pressure using He as the pore fluid.

## 5. Discussion

- Application of the calibration free missing attenuation method to rough-walled fractures gives the similar aperture estimations for both He and Kr gases (Fig. 4 and 5).
- Changes in average hydraulic aperture due to confining pressure are consistent with literature (see Fig. 7).
- While the average hydraulic aperture changes are comparable with literature, the CT scan shows heterogeneity of the fracture aperture distribution (Fig. 6), which will influence fluid channelization and, thus, rate of heat transfer and fluid flow in geothermal reservoirs.

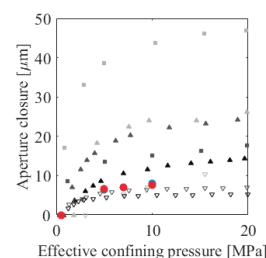


Fig. 7 Comparison of the whole core average hydraulic aperture measured with our CT results and previously published fluid flow experiments.

- He
- Kr
- Granite -Tsang and Witherspoon, 1981
- Marble - Tsang and Witherspoon, 1981
- ▲ Granite A - Vogler et al., 2016
- ▲ Granite B - Vogler et al., 2016
- ▲ Granite C - Vogler et al., 2016